1

Theoretical Backgrounds and Advances of Plasmonics

The field of nanoplasmonics is young but rich in phenomena that have inspired practical uses in physics, biomedicine, environmental monitoring, and national security

1.1 Introduction

When light irradiates on a solid materials, two kinds of electrons excitation will be formed in the materials. One is electron-hole pair excitation, which is called exciton. The other is the collective oscillation of electrons, which is known as plasmon. In physics, plasmon is a quantum of plasma oscillation that can be considered as a quasiparticle. Thus, plasmons are collective (a discrete number) oscillations of the free electron gas density [1, 2]. As a new type of exciton formed by the interaction between light and condensed matter, plasmon-related topic has become focus research in the frontier fields of micro-nano photonics. Ideally, plasmon is easy to excite without decay. However, all the materials exist in a certain medium environment, particularly for the low dimensional structure with rich surface and interfaces. When the dimensions of materials is comparable to the mean path of free electrons, Landau damping becomes the dominant loss source in plasmonics.

For the well-known metals, such as gold (Au) and silver (Ag), plasmons of these metals have significant spatial confinement and propagation loss due to the strong Landau damping effect and the scattering between plasmon and phonon [3]. In this chapter, some basic theory and experimental advances about plasmon will be presented, involving an overview of plasmon, dielectric function, propagation behavior, excitation and applications of surface plasmon.

1.2 Drude Model for Free Electron Gas

As one of the most basic models of solid physics, Drude (Drude-Lorentz) model described that the electrons in the metal are free around the fixed ion solid and

Plasmonic Metal Nanostructures: Preparation, Characterization, and Applications,
First Edition. Caixia Kan.

dispersed in the whole space of the metal, forming the so-called free electron gas [4]. The physical significance of the excitation at ω_p can be understood by considering the collective longitudinal oscillation of the conduction electron gas versus the fixed positive background of the ion cores in a plasma slab. To visualize a plasmon oscillation, it can be imagined that a metal was placed in an external electric field. A collective displacement of the electron cloud by a distance x leads to a surface charge density $\sigma = \pm n_e e x$ at the slab boundaries (n_e is number density of electrons). This establishes a homogeneous electric field $\boldsymbol{E}$. Thus, the displaced electrons experience a restoring force, and their movement can be described by the equation of Newtonian motion. If the electric field is removed, electrons oscillate back and forth at the plasma frequency until the energy is lost in some kind of resistance or damping. Inserting the expression for the electric field, we get the motion function (ε_0 is electric permittivity or dielectric constant of vacuum).

$$m\ddot{\boldsymbol{x}} = -e\boldsymbol{E} = -{}^{n_e e^2 \boldsymbol{x}}/_{\varepsilon_0} \tag{1.1}$$

Equation (1.1) can also be expressed by $\ddot{\boldsymbol{x}} + \frac{n_e e^2}{m\varepsilon_0}\boldsymbol{x} = 0$, in which plasmon vibrates at the same plasma frequency (ω_p) with $\omega_p^2 = \frac{n_e e^2}{m\varepsilon_0}$. ω_p is the plasma frequency of bulk materials. It exists in metals, semiconductors and insulators. But it cannot be excited nor can be observed by transverse light wave.

The plasma frequency ω_p can thus be recognized as the natural frequency of a free oscillation of the electron sea. The quanta of these charge oscillations are called plasmons (or volume plasmons) to distinguish them from surface and localized plasmons, which will be discussed in the next part. For most metals, the ω_p is in the ultraviolet regime ($\sim 10^{16}$ Hz), depending on details of the electrons density (n_e) and band structure. Light with frequencies less than ω_p will be reflected by the metals because the electrons in the metals screen the electric field of the light. If the light with frequencies above ω_p, the light will be transmitted through the metals because the electrons in the metals cannot respond fast enough to screen it. For most metals, the ω_p is in the ultraviolet region, making them shiny (reflective) in the visible range. Some metals, such as Cu and Au, have electronic interband transitions in the visible range, whereby specific light energies (colors) are absorbed, yielding their distinct color.

Due to the longitudinal nature of the excitation, volume plasmons do not couple to transverse electromagnetic waves. Plasmons can only be observed when high-speed electrons pass through a metal film or photons are reflected on the surface of the film. Another consequence is that their decay occurs only via energy transfer to single electrons, a process known as Landau damping.

Although Drude model is one classical free electron theory with Boltzmann distribution law under four approximations of independent electron, free electron, collision hypothesis and relaxation time, it can be well applied to explain the physical mechanism of surface plasmon and many experimental phenomena. Then the revised Drude-Sommerfeld model was proposed by taking Fermi-Dirac distribution law of quantum mechanics into Drude model.

1.3 Dielectric Function of the Free Electron Gas

For the materials in bulk, film or low dimensions, dielectric function is one important parameter in describing the photoelectronic properties of these structures. For some of the noble metals, interband effects already start to occur for energies of 1 eV. As examples, the real part (ε_r) and the imaginary part (ε_i) of the dielectric function for Au and Ag and Drude model fits to the data [5]. Clearly, this model is not adequate for describing either ε_r or ε_i at high frequencies. For the case of Au, its validity breaks down at the boundary between the near-infrared and the visible region.

With introduction of damping coefficient (γ), electron movement under the irradiation of electric field (ω) can be described by the equation of motion:

$$m\ddot{\boldsymbol{x}} + m\gamma\dot{\boldsymbol{x}} = -e\boldsymbol{E} \tag{1.2}$$

$$\boldsymbol{x} = \frac{e}{m(\omega^2 + i\gamma\omega)}\boldsymbol{E}(t) \tag{1.3}$$

According to the polarization of dielectric $\boldsymbol{D} = \varepsilon_0(1+\chi)\boldsymbol{E} = \varepsilon_0\varepsilon\boldsymbol{E}$, the polarization can be achieved.

$$\boldsymbol{P} = -n_e e\boldsymbol{x} = \chi\mathbf{E} = -\frac{n_e e^2}{m(\omega^2 + i\gamma\omega)}\boldsymbol{E}(t) \tag{1.4}$$

$\boldsymbol{P}$ describes the electric dipole moment per unit volume inside the material, caused by the alignment of microscopic dipoles with the electric field. The linear relationship between $\boldsymbol{D}$ and $\boldsymbol{E}$ is often implicitly defined using the dielectric susceptibility χ, particularly in quantum mechanical treatments of the optical response. The linear relationship between $\boldsymbol{D}$ and $\boldsymbol{E}$ via:

$$\boldsymbol{D} = \varepsilon_0(1+\chi)\boldsymbol{E} = \varepsilon_0\left(1 - \frac{\omega_p^2}{\omega^2 + i\gamma\omega}\right)\boldsymbol{E}(t) \tag{1.5}$$

Here the dielectric property as a function of frequency can be described as:

$$\varepsilon(\omega) = 1 - \frac{\omega_p^2}{\omega^2 + i\gamma\omega} \tag{1.6}$$

Then we can get real and imaginary parts of dielectric functions $\varepsilon_r(\omega) = 1 - \frac{\omega_p^2}{\omega^2+\gamma^2}$, $\varepsilon_i(\omega) = \frac{\omega_p^2\gamma}{\omega(\omega^2+\gamma^2)}$. Therefore, the refractive index of electrolyte is expressed in the form of $\tilde{N} = n + ik$. Here, n is refractive index coefficient, indicating the permittivity $\varepsilon_r = n^2 - k^2$. k is extinction coefficient related to the conductivity of the medium ($2nk = \sigma/\omega\varepsilon_0$). k presents the material loss during the relaxation (or Landau damping), in which the polarization cannot keep up with the change of external high-frequency electric field. Under the conditions that $\omega \gg \gamma$ or weak damping $\gamma = 0$, Eq. (1.6) can be written:

$$\varepsilon(\omega) = 1 - \frac{\omega_p^2}{\omega^2} \tag{1.7}$$

It can be taken as the dielectric function of the undamped free electron plasma. $\gamma > 0$ leads to damping of transmitted wave.

In general, $\varepsilon(\omega) = \varepsilon_r(\omega) + \varepsilon_i(\omega)$ complex-valued functions of frequency ω. ε can be experimentally determined for example via reflectivity studies and the determination of the complex refractive index $\tilde{N}$. As defined $\tilde{N} = \sqrt{\varepsilon}(\omega)$, $\tilde{N}$ is imaginary for $\omega < \omega_p$. A material with negative dielectric permittivity does not support propagation of electromagnetic waves; instead the electromagnetic field decays inside the materials with a certain depth and most of the incident energy is reflected. This behavior is the characteristic of metals, where the depth is typically around tens of nanometers. For this case, there is a strong interaction between metal and incident electromagnetic wave, known as absorption and scattering in the following parts of this chapter and Chapter 2.

Reflectivity of metal can be expressed by $R = \left|\frac{\tilde{N}-1}{\tilde{N}+1}\right|^2 = 1$, showing that metals have high reflectivity. Then $\tilde{N}$ is positive for $\omega > \omega_p$, and metal is only a conventional dielectric material for incident light.

For transverse waves, $\boldsymbol{K} \cdot \boldsymbol{E} = 0$, yielding the generic dispersion relation:

$$K^2 = \varepsilon(\boldsymbol{K}, \omega)\frac{\omega^2}{c^2} \tag{1.8}$$

From Eqs. (1.7) and (1.8), we can get the dispersion relation of volume plasmon $\omega^2 = \omega_p^2 + K^2c^2$. It is clear that this value is always larger than that in free space, as shown in Figure 1.1.

As it is discussed above, $\tilde{N}$ is real in value for $\omega > \omega_p$, while $\tilde{N}$ is imaginary for $\omega < \omega_p$, and $K = \frac{i}{C}\sqrt{\omega_p^2 - \omega^2}$, leading to rapid decay of electromagnetic waves in the material. The skin depth is defined as $\delta = c/\sqrt{\omega_p^2 - \omega^2}$, which determines whether the electromagnetic wave can propagate through the medium. For example, in

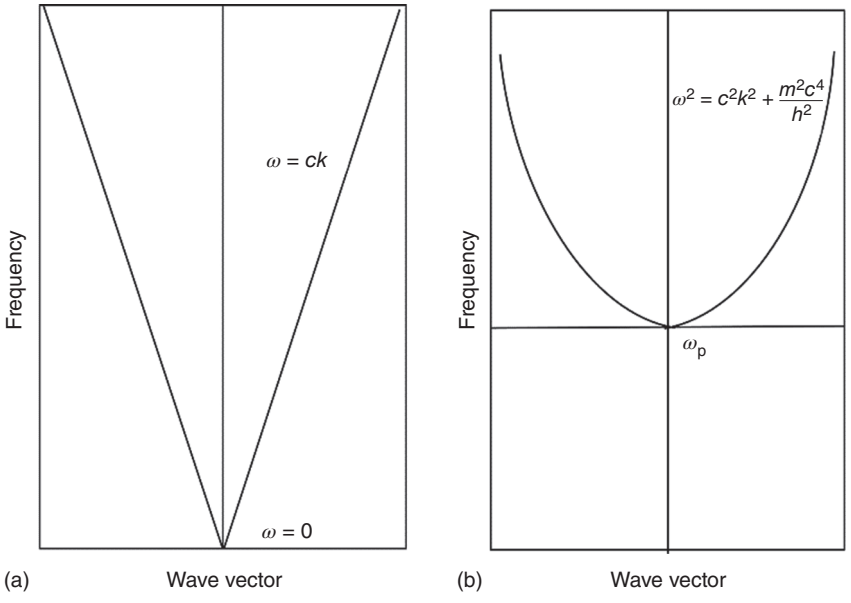

Figure 1.1 Dispersion of light in free space (a) and metals (b).

the ionosphere (50–500 km) above our ground, the plasmon density in the order of $10^{12-15}/m^3$, and the cut-off frequency (~10 MHz) is less than the TV band. Therefore, the TV electromagnetic signal can penetrate into this ionosphere and spread signal from the satellites. The free electrons in metals can also be regarded as plasmon. However, the frequency of visible light (~10 THz) is less than ω_p of metals (>100 THz), and visible light cannot penetrate most metals. As a result, most metals are silvery white for high reflectivity of visible light. In the metal-medium (or vacuum) system, the plasmons are confined strongly with light to surfaces, resulting in a surface polariton.

Actually, the electrons of metals are not free as described in the Drude model. The electrons have inherent frequency ω_0 and form restoring force that depends on the existing space or local structure. Therefore, the electron movement was revised into Eq. (1.9)

$$m\ddot{\boldsymbol{x}} + m\gamma\dot{\boldsymbol{x}} + m\omega_0^2\boldsymbol{x} = -e\boldsymbol{E} \tag{1.9}$$

We can get Eq. (1.10)

$$\varepsilon\left(\frac{1}{c}\frac{\partial}{\partial t}\right) = 1 - \frac{\omega_p^2}{\omega^2 + i\gamma\omega - \omega_0^2} \tag{1.10}$$

For practical purpose, the advantage of the Drude model is that it can easily be incorporated into time-domain based numerical solvers for Maxwell's equations. Its inadequacy in describing the optical properties of Au and Ag at visible frequencies can be overcome by replacing Eq. (1.6) with Eq. (1.10). Here, the interband transitions are thus described using the classical picture of a bound electron with resonance frequency ω_0.

In the Drude model for free electrons, the collective electrons vibration is a longitudinal wave mode due to the electrons vibration caused by electrostatic field force. The electric field caused by surface plasmons decays quickly after penetrating the interface, localizing in the range of a few nanometers on the surface.

1.4 Surface Plasmon Polaritons

Similar to the complex wave of water surface caused by liquid surface tension, there will be rich physical phenomena on the interface between metal and medium due to the breaking of symmetry. Surface plasmon is a special mode of plasmon due to the special boundary conditions on the surface.

Since plasmon was proposed as the quantization of classical plasma oscillation from a Hamiltonian for the long-range electron–electron correlations, most of their properties can be derived directly from Maxwell's equations [6]. When electromagnetic wave incidents on the interface between metal and medium, the coupling between collective electron vibration and incident light leads to the formation of near-field electromagnetic wave propagating along the metal surface. And resonance will occur if these two frequencies are the same. Under the resonance state, the energy of electromagnetic field is effectively transformed into

the collective vibration energy of free electrons on the metal surface. That is the well-known surface plasmon resonances (SPR).

There are also two modes of surface plasmon. One is longitudinal surface plasmon wave mode caused by electron oscillation, and the other one is confined to the surfaces that can interact with light to form propagating surface plasmon polaritons (SPPs). Polariton is the elementary excitation of the coupling vibration of photons and other quasiparticles. SPP has two excitation motions, charge motion (plasmon) and electromagnetic waves decayed at surface.

The electromagnetic field of SPP at a dielectric-metal interface is obtained from the solution of Maxwell's equations and the associated boundary conditions. To introduce the main characteristics of SPP, we consider a system consisting of a dielectric material, characterized by an isotropic dielectric constants ε_2 (real and positive), in the half-space $z > 0$, and a metal in the half-space $z < 0$, characterized by complex dielectric function $\varepsilon_1(\omega) = \varepsilon_r(\omega) + \varepsilon_i(\omega)$.

Using the continuity of electric field at the interface, we can get the electromagnetic field of SPP at the dielectric-metal interface with the polarization direction of the incident light parallel to the incident plane. From the Maxwell's electromagnetic field theory, we can obtain the following equations:

$$\begin{cases} \nabla \times H_i = \varepsilon_i \dfrac{\partial}{\partial t} E_i \\ \nabla \times E_i = -\mu_0 \dfrac{\partial}{\partial t} H_i \\ \nabla \cdot \varepsilon_i E_i = 0 \\ \nabla \cdot H_i = 0 \end{cases} \tag{1.11}$$

$i = 1$ at $z < 0$, and $i = 2$ at $z > 0$

Then we can get the s-polarized wave (TE mode) with $\frac{\partial}{\partial t} = i\omega$

$$\nabla^2 \boldsymbol{E} + K^2 \varepsilon \boldsymbol{E} = 0 \tag{1.12}$$

We then consider a p-polarized (transverse magnetic or TM) wave in this structure that propagates in the x-direction.

$$\begin{cases} \dfrac{\partial^2 \boldsymbol{E}_y}{\partial z^2} + \left(K^2 \varepsilon - \boldsymbol{K}_x{}^2\right) \boldsymbol{E}_y = 0 \\ \boldsymbol{H}_x = i \dfrac{1}{\omega \mu_0} \dfrac{\partial \boldsymbol{E}_y}{\partial z} \\ \boldsymbol{H}_z = \dfrac{K'}{\omega \mu_0} \boldsymbol{E}_y \end{cases} \tag{1.13}$$

$$\begin{cases} \dfrac{\partial^2 \boldsymbol{H}_y}{\partial z^2} + \left(K^2 \varepsilon - \boldsymbol{K}_x{}^2\right) \boldsymbol{H}_y = 0 \\ \boldsymbol{E}_x = -i \dfrac{1}{\omega \varepsilon \mu_0} \dfrac{\partial \boldsymbol{H}_y}{\partial z} \\ \boldsymbol{E}_z = -\dfrac{K'}{\omega \varepsilon \varepsilon_0} \boldsymbol{H}_y \end{cases} \tag{1.14}$$

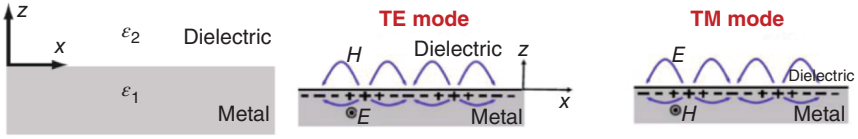

Figure 1.2 Dispersion of transverse electric TE mode and transverse magnetic TM mode on the dielectric-metal interface.

For the TE case, k_1 and k_2 are wave vectors in metal and medium along z direction. We now consider an s-polarized (transverse electric or TE) wave in the structure depicted in Figure 1.2. In a wave of this polarization, it is the electric vector that is perpendicular to the plane of incidence. The solutions of Maxwell's equations that are wavelike in the x-direction localized to the interface can be written as:

$$\begin{cases} \boldsymbol{E}_y(z) = A_1 \mathrm{e}^{i\boldsymbol{K}_x x}\mathrm{e}^{k_{1z}z} \\ \boldsymbol{H}_x(z) = iA_1 \frac{1}{\omega\mu_0} k_{1z}\mathrm{e}^{i\boldsymbol{K}_x x}\mathrm{e}^{k_{1z}z} \quad Z<0 \\ \boldsymbol{H}_z(z) = A_1 \frac{K'}{\omega\mu_0}\mathrm{e}^{i\boldsymbol{K}_x x}\mathrm{e}^{k_{1z}z} \end{cases} \tag{1.15}$$

$$\begin{cases} \boldsymbol{E}_y(z) = A_2 \mathrm{e}^{i\boldsymbol{K}_x x}\mathrm{e}^{-k_{2z}z} \\ \boldsymbol{H}_x(z) = -iA_2 \frac{1}{\omega\mu_0} k_{2z}\mathrm{e}^{i\boldsymbol{K}_x x}\mathrm{e}^{-k_{2z}z} \quad Z>0 \\ \boldsymbol{H}_z(z) = A_2 \frac{K'}{\omega\mu_0}\mathrm{e}^{i\boldsymbol{K}_x x}\mathrm{e}^{-k_{2z}z} \end{cases} \tag{1.16}$$

The continuity of the tangential components of the electric ($\boldsymbol{E}_y$) and magnetic fields ($\boldsymbol{H}_x$) across the interface $z = 0$ yields the pair of equations.The solution of this equation is $A_1 = A_2 = 0$. Thus an s-polarized SPP (TE mode) cannot exist in the structure depicted.

Therefore, we only consider a p-polarized (transverse magnetic or TM) wave in this structure that propagates in the x direction. In a wave of this polarization the magnetic vector is perpendicular to the plane of incidence – the plane defined by the direction of propagation and the normal to the surface. The solutions of Maxwell's equations that are wavelike in the x direction and whose amplitudes decay exponentially with increasing distance into each medium from the interface $z = 0$ can be written as:

$$\begin{cases} \boldsymbol{H}_y(z) = A_1 \mathrm{e}^{i\boldsymbol{K}_x x}\mathrm{e}^{k_{1z}z} \\ \boldsymbol{E}_x(z) = -iA_1 \frac{1}{\omega\varepsilon_1\varepsilon_0} k_{1z}\mathrm{e}^{i\boldsymbol{K}_x x}\mathrm{e}^{k_{1z}z} \quad Z<0 \\ \boldsymbol{E}_z(z) = -A_1 \frac{K'}{\omega\varepsilon_1\varepsilon_0}\mathrm{e}^{i\boldsymbol{K}_x x}\mathrm{e}^{k_{1z}z} \end{cases} \tag{1.17}$$

$$\begin{cases} \boldsymbol{H}_y(z) = A_2 \mathrm{e}^{i\boldsymbol{K}_x x}\mathrm{e}^{-k_{2z}z} \\ \boldsymbol{E}_x(z) = iA_2 \frac{1}{\omega\varepsilon_2\varepsilon_0} k_{2z}\mathrm{e}^{i\boldsymbol{K}_x x}\mathrm{e}^{-k_{2z}z} \quad Z>0 \\ \boldsymbol{E}_z(z) = -A_1 \frac{K'}{\omega\varepsilon_2\varepsilon_0}\mathrm{e}^{i\boldsymbol{K}_x x}\mathrm{e}^{-k_{2z}z} \end{cases} \tag{1.18}$$

The boundary conditions at the plane $z = 0$ yield the pair of equations:

$$\begin{cases} A_1 = A_2, \frac{k_{2z}}{k_{1z}} = -\frac{\varepsilon_2}{\varepsilon_1} \\ k_{1z} = \sqrt{K_x{}^2 - K^2\varepsilon_1} \\ k_{2z} = \sqrt{K_x{}^2 - K^2\varepsilon_2} \end{cases} \tag{1.19}$$

Here we can write wave vector in the x direction.

$$K_x = K\sqrt{\frac{\varepsilon_1\varepsilon_2}{\varepsilon_1 + \varepsilon_2}} = \frac{\omega}{c}\sqrt{\frac{\varepsilon_1\varepsilon_2}{\varepsilon_1 + \varepsilon_2}} \tag{1.20}$$

In the region of $z < 0$, k_z determines the decay of the electromagnetic field with increasing distance from the surface.

Surface plasmon occurs at the interface of a material exhibiting positive part in a dielectric constant (such as vacuum, air, glass, and other dielectrics) and a metal (or heavily doped semiconductor) whose real part of permittivity is negative at the given frequency of light. The dispersions of bulk plasmon, SPP at a dielectric-metal interface, light in air and in the dielectric medium is shown in Figure 1.3. In addition to opposite sign of the real part of the permittivity, the magnitude of the real part of the permittivity in the negative permittivity region should typically be larger than the magnitude of the permittivity in the positive permittivity region, otherwise the light is not bound to the surface (i.e. the surface plasmons do not exist).

For the existence of surface plasmon wave, the wave vector must be a positive value. Due to the facts of $\varepsilon_1 < 0$, $\varepsilon_2 > 0$, and $|\varepsilon_1| > \varepsilon_2$, it can be seen that the surface wave vector $\boldsymbol{K}_x$ is always larger than $\boldsymbol{K}$ for the incident light of any frequency. $\boldsymbol{K}_z$ must be an imaginary number,and electromagnetic field of the SPP decays

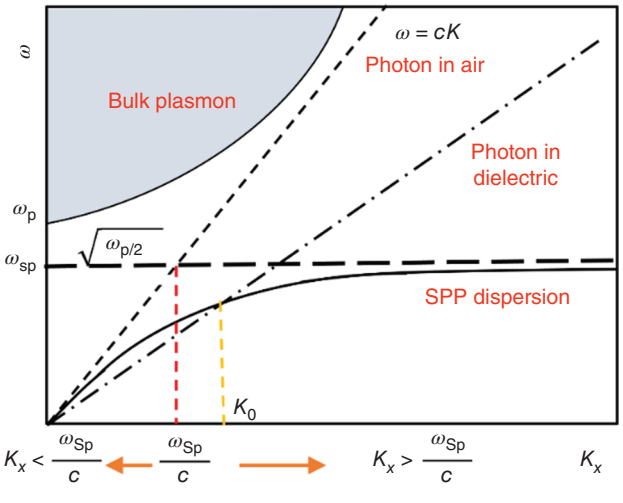

Figure 1.3 Dispersion of SPP at a dielectric-metal interface. Also plotted is the dispersion of light in air and in the dielectric medium, and the corresponding surface plasmon frequency.

exponentially in the z direction into the dielectric medium in contact with the metal. Consequently, the SPP cannot radiate light into the dielectric medium, and cannot be excited with conventional illumination from the adjacent dielectric. Moreover, the frequency of the surface plasmon is also the limiting frequency of the SPP with $\boldsymbol{K}_x \to \infty$.

Thus, the existence of SPs depends entirely on the fact that dielectric function $\varepsilon(\omega)$ has a negative real part ($\varepsilon_1 < 0$). The SPs are well pronounced as resonances when the losses are small enough, i.e. $\lfloor \varepsilon_1 \rfloor \gg \varepsilon_2$. This is the well-known property of a good plasmonic metal. We will define the substance as a good plasmonic metal if these two properties are satisfied simultaneously.

1.5 Plasmon at Metal-Vacuum Interface

For the metal-vacuum interface with $\varepsilon_2 = 1, K = \frac{\omega}{c}$, when $\boldsymbol{K}_x \longrightarrow \infty$, $\varepsilon_1 + \varepsilon_2 = 0$, we can see the relation between the bulk plasmon and SPP in the Drude model Eq. (1.7)

$$\omega_{\mathrm{sp}} = \sqrt{\frac{\omega_{\mathrm{p}}}{2}} \tag{1.21}$$

For the metal-dielectric interface, $\varepsilon_2 = \varepsilon_{\mathrm{d}}, K = \frac{\omega}{c}\sqrt{\varepsilon_{\mathrm{d}}}$ in dielectric, and $\omega = cK/\sqrt{\varepsilon_{\mathrm{d}}}$. This wave vector k_0 equals to one value of SPP.

As discussed above, the metal film is not treated as a conductor as bulk metal in electromagnetic field. The metal films and nanostructures in the following chapters will be treated as special dispersive medium with polarization property in electromagnetic field. Under this case, the SPP mode for metals is obtained.

1.5.1 Propagation Length

As the electromagnetic field of the SPP decays exponentially along the z direction into the dielectric medium in contact with the metal. It is necessary to know the propagation length and depth.

From Eq. (1.10), it is clear that $\varepsilon(\omega) = \varepsilon_{\mathrm{r}}(\omega) + \varepsilon_{\mathrm{i}}(\omega)$ and wave vector has real and imaginary parts for the metals. For the metal-vacuum interface, we can see that the real and imaginary parts of wave vectors are as following:

$$K_{x\mathrm{r}} \approx \frac{\omega}{c}\left(\frac{\varepsilon_{1\mathrm{r}}}{\varepsilon_{1\mathrm{r}}+1}\right)^{1/2} \tag{1.22}$$

$$K_{x\mathrm{i}} \approx \frac{\omega}{c}\frac{\varepsilon_{1\mathrm{i}}}{2\varepsilon_{1\mathrm{r}}^2}\left(\frac{\varepsilon_{1\mathrm{r}}}{\varepsilon_{1\mathrm{r}}+1}\right)^{3/2} \tag{1.23}$$

Due to Ohmic losses in the metal, characterized by the imaginary part of the dielectric function of the metal, the energy carried by a SPP decays exponentially as the SPP propagates along the planar dielectric-metal interface. The decay length, called the energy propagation length L_{sp} is determined by the imaginary part of

the SPP wavenumber. The propagation length along the metal–vacuum interface is defined as $L_{sp} = (2K_{xi})^{-1}$. For example, the propagation lengths for Au and Ag are $L_{Au} = 14$ μm and $L_{Ag} = 44$ μm with the irradiation 633 nm light (the ε of metals of this frequency can be referred to Ref. [5]).

Plasmons or bulk plasmons cannot be coupled with light waves and can only be excited by particle collisions. In metals (as mentioned Au and Ag) with large number of free electrons, plasmons have very high propagation loss due to the strong Landau damping effect and the scattering between plasmons and phonons. While for two-dimensional materials, the plasmons attenuation is greatly suppressed because they are confined to the plane. As typical representative two-dimensional materials, graphene and black phosphorus become extremely popular plasmon materials [7].

1.5.2 Propagation Depth (or Skin Depth)

From Eq. (1.19) the wave vector in the z direction can be written as:

$$\begin{cases} k_{1z} = \dfrac{\omega}{c}\sqrt{\dfrac{-\varepsilon_1^2}{\varepsilon_1 + \varepsilon_2}} \\ k_{2z} = \dfrac{\omega}{c}\sqrt{\dfrac{-\varepsilon_2^2}{\varepsilon_1 + \varepsilon_2}} \end{cases} \tag{1.24}$$

The skin depth is defined as $\delta_i = 1/k_i$. It is clear that the penetration depth in vacuum is greater than that in metals. SPP is an evanescent wave along the normal direction of the interface. Figure 1.4 shows the schematic diagram and FDTD simulation diagram for SPP propagation in medium, metals and their interfaces [8]. The finite skin depth of real metals leads to an effect related to nanoplasmonic confinement. For example, the skin depths for most metals (δ_{metal}) are about several to tens of nanometers [2], δ_{diel} is in the range of 250–1000 nm, and δ_{SPP} is about 2–20 μm with the irradiation 500 nm light. The characteristic lengths of Ag plasmons are slightly larger than those of other metals. For electromagnetic wave with frequency of 50 MHz ($\lambda = 6$ m), the skin depth is more than one hundred meters for dry soil of poor conductivity, while the skin depth is greatly reduced to millimeters for sea water. Thus, submarines under the sea cannot receive radio waves, and we can receive the signal under the subway.

The common presumption that electromagnetic radiation cannot be concentrated or confined to a region whose size is less than half the incident wavelength. It is obvious that the minimum volume of an optical field localized in a cavity – bounded by three pairs of ideal mirrors with size of $\lambda/2$. How can an optical field be localized 6–7 orders of magnitude tighter on the scale of 1 nm? From the above skin depth, the particles should be smaller than the metal's skin depth – how deeply the optical radiation penetrates the metal. That depth is roughly 25 nm for Au, Ag, and Cu over the entire optical and most of the IR region [2]. On the minimum end, the particles should not be smaller than the so-called nonlocality length about 2 nm. On the scale of 2–20 nm, an incident light wave is always a plane wave, and no light focusing in the optical far-field is possible.

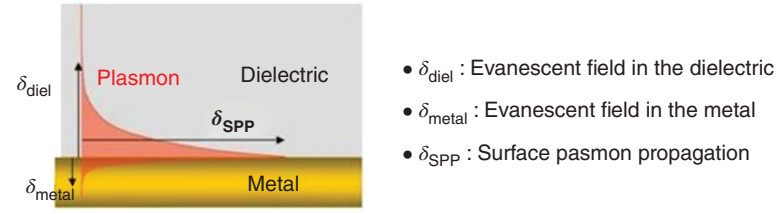

(a)

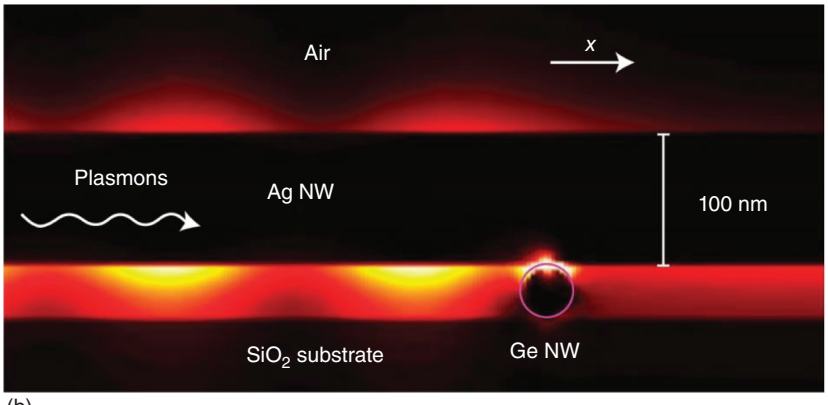

(b)

Figure 1.4 Schematic diagram and simulation diagram for SPP propagation in medium-metals (a) and their interfaces. δ_{diel} and δ_{metal} evanescent wave (b) FDTD simulation of electric-field intensity. Ag nanowire diameter = 100 nm, Ge nanowire diameter = 40 nm. Source: Falf et al. [8]/Reproduced with permission from © 2009 Springer Nature.

1.6 Excitation and Detection of SP

Generally, surface plasmon has momentum as a quasiparticle. SP can be excited by electrons or photons. The response function of material to external field is dielectric function. The very small momentum of light can be ignored. The momentum conservation also limits the coupling between plasmon and light. Usually, the bulk plasmon is the quantum of longitudinal electron-density wave within the bulk metal, and it cannot be excited by transverse electromagnetic plane waves. It can only be excited by electron beam. While the SP, also quantum of longitudinal electron-density waves, confined to the metal-dielectric interface, and it is often excited using dielectric prism coupled with a thin metal film, near-field optics and other methods. Here optical and electrical excitation of SP will be presented. As an important content of this book, localized surface plasmon (LSP) of metal nanoparticles will also be delivered.

1.6.1 Optical Excitation of SP

The reason that the SPs can be optically excited is because their relevant physical property are the same. SPs are Bosons with spin of 1 as photons do. At the same

time, SPs are electrically neutral excitations. SPs are the most collective material oscillations known in nature, and they interact very weakly with one another. Therefore, they can undergo stimulated emission, accumulating in a single mode in large numbers.

In order to excite an SP by p-polarized light incident on a planar metal surface from the adjacent dielectric medium, the frequency of the incident light must equal the frequency of the SP. From the SP dispersion relation or Figure 1.3, we can see that light incident from air cannot be directly coupled with SPP mode because the wave vector of SP is larger than that in air. The SP can be excited with the assistance of special experimental arrangements or structures for matching the wave vector. Therefore, several devices (Figure 1.5) have been designed to provide the necessary wave vector conservation, including reflection geometry (Kretschmann and Otto configurations), scanning near-field optical microscopy (SNOM), diffraction effects (grating couples) surface roughness and scattering particles [9].

In the Kretschmann configuration, a metal film is illuminated through a dielectric prism at an angle of incidence greater than the critical angle for total internal reflection. The wavevector of light is increased in the optically more dense medium. At the angle of incidence at which the in-plane component of the photon wave-vector in the prism coincides with the SPP wave vector at the air-metal interface, resonant light tunneling through the metal film occurs, and light is coupled to surface polaritons. Figure 1.6a presents the detailed wave vector in the Kretschmann geometry. Under these resonant conditions, a sharp minimum is observed in the reflectivity from the prism-metal interface as light can be coupled to SPP. Since the SPP field is concentrated close to a metal surface, it is significantly enhanced at the surface. With the increase of the metal film thickness the efficiency of the SPP excitation (and the

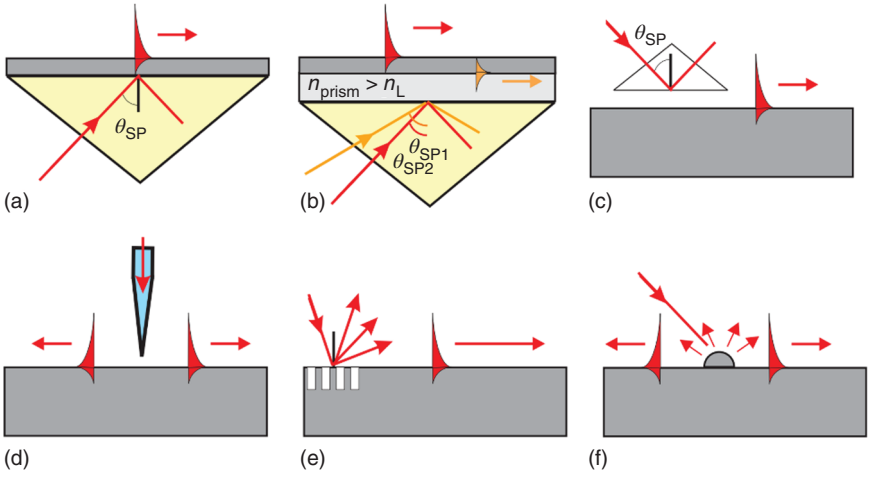

Figure 1.5 SP excitation configurations: (a) Kretschmann geometry, (b) two-layer Kretschmann geometry, (c) Otto geometry, (d) excitation with a SNOM probe, (e) diffraction on a grating, and (f) diffraction on surface features. Source: Reproduced from Zayatsa et al. [9]/with permission of Elsevier.

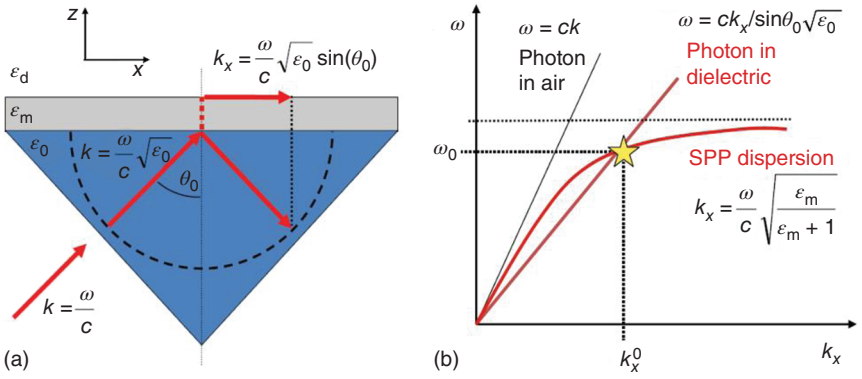

Figure 1.6 (a) Wave vector dispersion in the Kretschmann geometry. (b) Typical SPP dispersion at the metal-dielectric interface.

field enhancement) decreases with increasing the distance. Usually, an additional dielectric layer with a refractive index smaller than the one of the prism should be deposited between the prism and the metal film. In this two-layer geometry, the photon tunneling through this additional dielectric layer can also provide excitation of SPP on the inner interface, as shown in Figure 1.6b.

With the development of scanning probe techniques, it become possible to study SPs locally on a surface using SNOM. In particular, SNOM provides an opportunity to probe the SP field directly over the SP existing surface. The application of SNOM to SP studies introduced a new technique that provides the possibility to excite SP locally at a given surface. Using illumination through a SNOM fiber tip, circular SP waves can be locally launched at the surface. This configuration can be treated as either a diffraction or a tunneling mechanism of SP excitation. This technique allows local and precise excitation of SPs at the SNOM tip.

Plasmon can be excited by particle collisions without any special arrangements, although it cannot be coupled with light waves. Light scattering and absorption by a sphere surely constitute the most evolved model for light scattering by obstacles. On a randomly rough surface, the SP excitation conditions can be achieved. The rough surface can be consisted of small sized particles, and the SP is highly localized near the particles, as known LSPs. Here we briefly present the concept of LSP. LSP can be supported by subwavelength features on a small sized metal particle surface where the LSP can decay into SP. As a result, LSP can be excited by SPP. These results in a significant enhancement of SPP scattering by surface defects if the frequency of SP and the resonant frequency of LSP are close to each other.

This is possible since in the near-field region diffracted components of light are all wave vectors (Figure 1.5f). The problem with random roughness is ill-defined nonresonant SP excitation, resulting in a low efficiency of light-to-SP coupling. Such nonresonant SP excitation processes result in a complex field distribution over the surface due to the interference of the SPPs excited on different interfaces of the film and the non-coupled illuminating light. LSP resonances play a significant role in the

behavior of SPP on rough surfaces if their frequency is close to the SP frequency, as will be discussed in Chapter 2. Over the last few decades, plasmonics has brought us new opportunities to control light at wavelength scales, thus leading to many inspiring applications, such as super resolution imaging beyond the diffraction limit, new kind of optical sensors with enhanced performance.

1.6.2 Electrical SPP Excitation

In addition to optical illumination, energized electrons have also been employed to excite metal plasmons, such as high energy free electrons, inelastic electron tunneling, and a modest electric field [10, 11]. Excitation by electrons is created by firing electrons into the bulk of a metal. As the electrons scatter, energy is transferred into the bulk plasmon. The component of the scattering vector parallel to the surface results in the formation of SPP. With the development of nano-fabrication techniques, on-chip electrically-driven plasmonic circuitries have gained great attention in the post-Moore era for they hold the promise to combine both the small device footprint of electronic circuitry and the large information capacity. Recently, direct electrical excitation of SPP via inelastic electron tunneling in metal–insulator–metal junctions has reemerged as a promising ultrafast source to drive the integrated plasmonic circuitries.

Since 2003, plasmonics has facilitated the realization of coherent nanolasers [12], plasmon enhance diodes [13]. Naturally, the next step is to realize the electrically driven plasmon sources that can be integrated with optoelectronic circuitry. In 2012, Fan et al. present an experimental demonstration of electrically driven GaAs nanowire light sources integrated with plasmonic Ag nanostrip waveguides [14]. SPPs are experimentally demonstrated and analyzed with the help of full-field electromagnetic simulations, as indicated by Figure 1.7. They also found that light leaking out of plasmonic waveguide bend and emerges from the Y-splitter junction, and suggested that making splitting junction as “sharp” as possible can minimize splitting losses.

In 2019, Yang et al., designed and experimentally demonstrated an electrically driven UV plasmonic laser at room temperature in a p-GaN/MgO/ZnO/MgO/Ag structure, as shown in Figure 1.8. [15] This structure includes an Ag/MgO/ZnO MIS hybrid plasmonic waveguide, in which strong optical confinement and relatively low metal loss can be satisfied simultaneously. In the proposed structure, holes are injected into ZnO layer from p-GaN, and electrons are injected from Ag film through MgO gap layer. An additional electron blocking MgO layer has been introduced at the interface between the gain region and the GaN layer to enhance the emission from ZnO by blocking electrons in the ZnO from entering into the p-GaN. This plasmonic laser device represented the state-of-the-art performances inelectrically driven plasmonic lasers.

Neutens et al. demonstrated an integrated electrical source of confined SPPs in LED-MIM device [16]. The electrical injection of SPPs inside an MIM waveguides can combine high spatial field confinement and propagation lengths of several micrometers. Since the metallic cladding layers ensure that the fields are confined

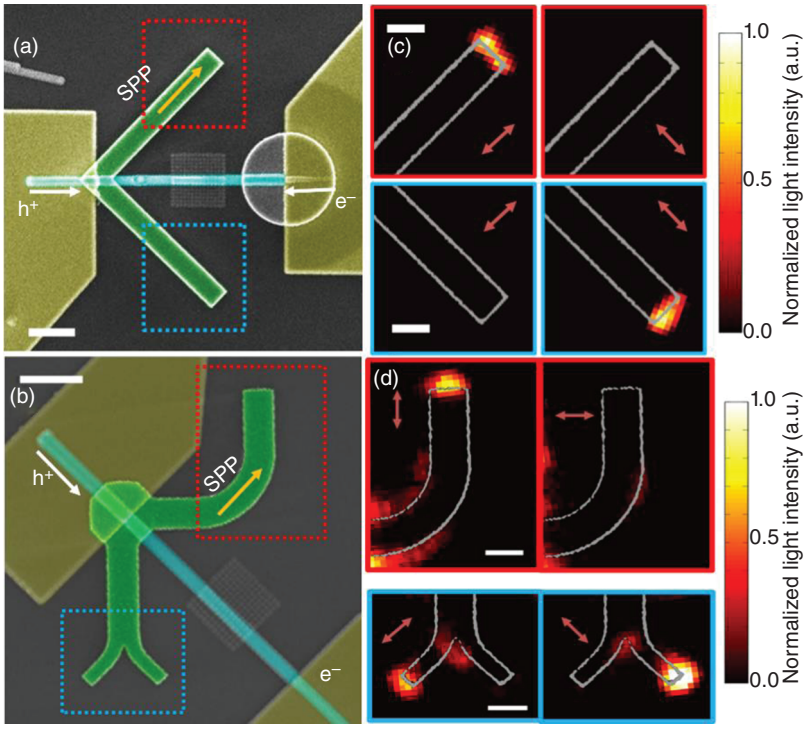

Figure 1.7 (a, b) Scanning electron microscopy (SEM) image of the structures (straight strip, bend, and Y-shape) collected by CCD camera under lamp illumination with false-color highlighting the different components: yellow is for electrical contacts, cyan is for GaAs nanowire, and green indicates the Ag strip waveguides. Scale bar is 2 μm. (c, d) Detailed spatial distribution of the scattered light intensity near the terminations of waveguides with different shapes when only collecting light with the electric field component polarized along and perpendicular to the waveguides, respectively. Scale bars are 1 μm. Source: Fan et al. [14]/Reproduced with permission from © 2012, American Chemical Society.

within the waveguide, one can easily separate plasmonic effects from any other nonplasmonic background radiation. The working principle of the LED-MIM device was clearly demonstrated. When the polarization of the dipole is set in plane and perpendicular to the slit axis, light generated in the quantum well excites a local plasmonic mode inside the injection slit. This local mode couples efficiently to a propagating mode inside the MIM waveguide.

The injection and detection slits in the waveguide partially reflect surface plasmons, resulting in a Fabry–Perot cavity inside the MIM waveguide. Only light with transverse magnetic polarization can be emitted at the detection slit. They also observed theoretically expected an exponential decay of the SPPs along the waveguide, caused by the Ohmic losses inside the metal layers of the metallic slot waveguide. It is well-known that the nonradiative plasmonic decay can also generate hot carriers from metal nanostructures. Sun et al. reported on the incandescent-type light source composed of Au NRs decorated with single Ga-doped ZnO microwire, as illustrated by Figure 1.9 [17].

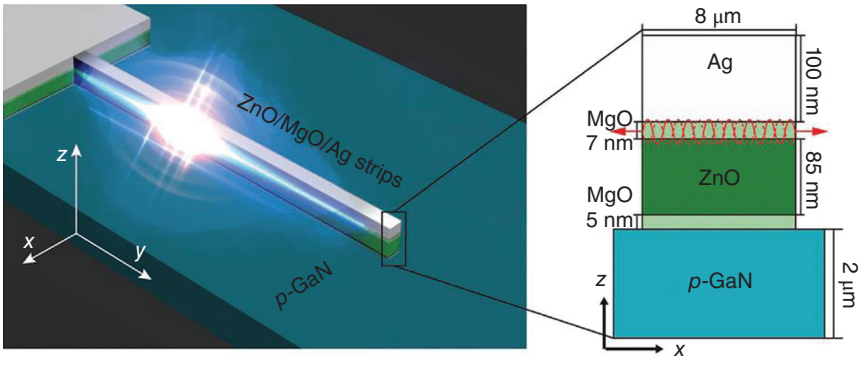

Figure 1.8 The schematic diagram of electrically driven plasmonic laser based on p-GaN/MgO/ZnO/MgO/Ag structure. Inset illustrates the SPPs feedback diagram in the ZnO/MgO/Ag cavity. Source: Reproduced from Yang et al. [15] © 2019/with permission of John Wiley and Sons Inc.

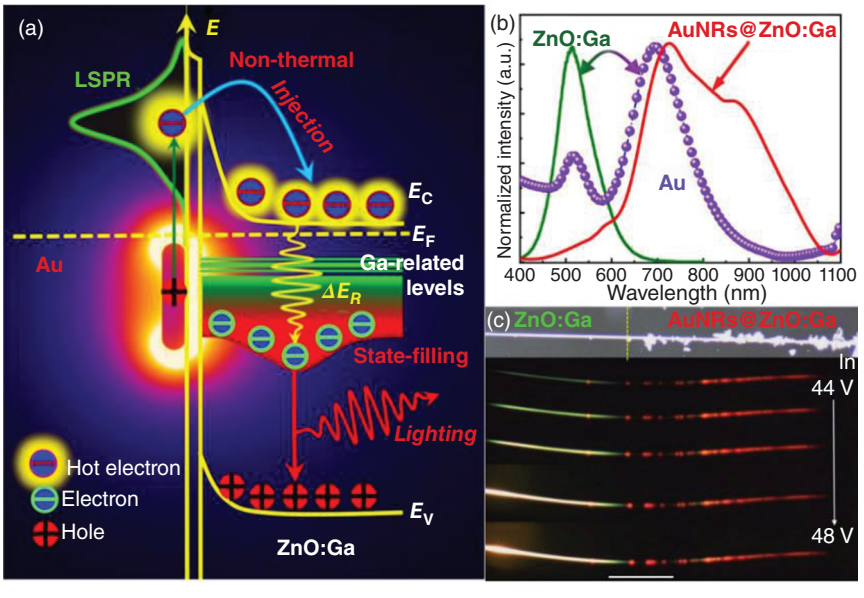

Figure 1.9 (a) Schematic diagram of the working principle of bright visible light emitting from electrically biased single AuNRs@ZnO:Ga MW-based incandescent-type light source. (b) Normalized intensities of the EL spectrum from single bare ZnO:Ga MW-based fluorescent light source, the EL spectrum from single AuNRs@ZnO:Ga MW-based fluorescent light source, and the extinction spectrum of the deposited Au NRs. (c) Optical microscopic images of bright visible light emitting from electrically driven single ZnO:Ga MW prepared with partial Au NRs decoration (scale bar, 300 μm). Source: Sun et al. [17]/Reproduced with permission from © 2020, Optica Publishing Group.

Under a sufficiently strong electric field ($\sim 10^6 \mathrm{V\,m^{-1}}$), hot spots could be produced owing to the extremely poor heat dissipation of semiconductor. Then collective oscillation of the free electrons in Au NRs can be electrically excited. Through nonradiative plasmonic decay, Au NR plasmons can transfer their energies into oscillating higher-energy electrons, leading to formation of hot electrons. Especially once the hot electron possessed the energy up to plasmon frequency, Au-nanorod plasmons inducing the generation of nonequilibrium distribution of hot electrons can lead to the state-filling effect in the energy-level configuration of ZnO:Ga, which can be employed to dominate the near-infrared emission characteristics from single AuNRs@ZnO:Ga microwire based incandescent light source, as shown in Figure 1.9b,c. Nonradiative decay of surface plasmons generates hot carriers in metal nanostructures that can be injected into neighboring semiconductor micro/nanostructures. Thus wavelength-tunable incandescent-type emissions can be achieved from visible to near-infrared region adjusting the aspect ratios of the Au NRs. Such working principle on the generation of hot carriers has been utilized to construct and further enhance the electronic and optoelectronic devices. The plasmon-enhanced optoelectronic device will be discussed in Chapter 9.

Optically excited SPs are featured by dipolar charge oscillations and they can be understood as bright SPs due to their dipole-active character. Bright SPs can be further tailored in Vis-NIR regime by controlling the size and morphology of noble metal nanoparticles. But dark surface-plasmon modes cannot be excited by optical means. Although SNOM can excite SPP locally at a given surface, this technique can hardly reach a spatial resolution. In contrast, electron-energy-loss spectroscopy (EELS) performed in a scanning transmission electron microscope (STEM) routinely provides nanometer spatial resolution by focusing a subnanometer electron beam on nanoparticles and analyzing the energy losses of the electrons. Chu et al. reported that STEM-EELS can excite bright and dark SP modes in metal monomer and coupled nanochain structures [18]. Upon external illumination with the electric field polarized along the dimer axis, the induced charge oscillation thus involves a longitudinal coupled SP along the long axis and a transversal coupled SP perpendicular to that axis. Compared to the SP excitation energy of a single spherical nanoparticle, the SP excitation of coupled dimer behaviors red- and blue-shifting, which will be discussed in the following part of "detection of surface plasmon" using EELS.

These types of SP-distribution features should be observable by tilting the sample and measuring the spectra at various angles of electron incidences. In such cases, STEM-EELS should then be able to provide information on the local polarization of the SP near fields, as described in Chapter 3.

1.6.3 Localized Surface Plasmon of Nanoparticles

In addition to SPP and surface plasmons at a planar dielectric-metal interface, as shown in Figure 1.5f for the photon excitation of SPP, it can be seen that the isolated surface defects, such as a groove, a particle, a slit or a corrugation on a planar surface provides a mechanism by which free-space radiation and SPs can exchange energy

and hence couple. In the localized space, electromagnetic excitations can exist in nanometer sized metal objects of various shapes.

As discussed above, for materials with negative dielectric permittivity (characteristic behavior of metals), the most of the incident irradiation is reflected and incident electromagnetic field decays inside the materials with a depth of a few tens nanometers. But for a nanoparticle with size smaller than the depth size, optical fields are able to penetrate its entire volume and drive SP oscillations. It is the skin depth that determines the characteristic length scale in nano-optics and makes the nanoscale important. Plasmonic nanoparticles can couple with electromagnetic radiation of wavelengths far larger than the particle due to the nature of the dielectric-metal interface.

For the case of SP oscillations, conduction electrons in metal or metal-doped semiconductor nanomaterials can be coherently excited by incident light to collectively oscillate at metal/dielectric interfaces. For metal nanoparticles, surface waves can be excited directly by optical excitation, leading to the conception of metallic or "plasmonic" nanostructures as nanoscale optical components. Such surface excitations in bounded geometries are the well-known LSPs. Plasmons are the oscillations of free electrons that are the consequence of the formation of a dipole or multipole in the material under electromagnetic waves. The electrons migrate in the material to restore its initial state. However, the light waves oscillate, leading to a constant shift in the dipole or multipole that forces the electrons to oscillate at the same frequency as the light. This coupling only occurs when the frequency of the light is equal to or less than the plasma frequency and is greatest at the plasma frequency that is therefore called the resonant frequency. Under the resonant frequency, plasmonic nanoparticles exhibit interesting scattering, absorbance, and coupling properties.

For metal objects of various shapes with sizes smaller than the light wavelength, absorption and scattering response of light by particles can be characterized after solving Maxwell's equations. In 1908, Gustav Mie obtained an analytical solution for single spherical particles by solving the scattering of a monochromatic plane wave by a homogeneous dielectric sphere of arbitrary size in a homogeneous medium [19]. The theory of plane-wave scattering by a homogeneous isotropic sphere is also called Lorenz–Mie theory or Lorenz–Mie–Debye theory for their contributions to solving this problem [20, 21]. Briefly, the polarization of dipole when one uniform spherical particle with a volume of V was irradiated under the plane light.

$$\chi = 3V\frac{\varepsilon - \varepsilon_{\mathrm{m}}}{\varepsilon + 2\varepsilon_{\mathrm{m}}} \tag{1.25}$$

Then the expressions for the optical cross, such as extinction section σ_{ext}, scattering section σ_{sca}, and absorption section σ_{abs}, can be obtained ($\sigma_{\mathrm{ext}} = \sigma_{\mathrm{sca}} + \sigma_{\mathrm{abs}}$).

$$\sigma_{\mathrm{sca}} = \frac{k^4}{6\pi}|\chi|^2 = C_1\frac{a^6}{\lambda^4}\left|\frac{\varepsilon - \varepsilon_{\mathrm{m}}}{\varepsilon + 2\varepsilon_{\mathrm{m}}}\right|^2 = C_1\frac{a^6}{\lambda^4}\frac{(\varepsilon_1 - 2\varepsilon_{\mathrm{m}})^2 + \varepsilon_2^2}{(\varepsilon_1 + 2\varepsilon_{\mathrm{m}})^2 + \varepsilon_2^2} \tag{1.26}$$

$$\sigma_{\mathrm{abs}} = k\mathrm{Im}(\chi) = C_2\frac{a^3}{\lambda}\left|\frac{\varepsilon - \varepsilon_{\mathrm{m}}}{\varepsilon + 2\varepsilon_{\mathrm{m}}}\right|^2 = C_2\frac{a^3}{\lambda}\frac{\varepsilon_{\mathrm{m}}\varepsilon_2}{(\varepsilon_1 + 2\varepsilon_{\mathrm{m}})^2 + \varepsilon_2^2} \tag{1.27}$$

where $C_1 = 128\pi^3/3$, $C_2 = 32\pi^2$, a presents the radius of particle. When the particle size is smaller than the light wavelength, we can see $\frac{a^6}{\lambda^4} = a^2\frac{a^4}{\lambda^4} \ll a^2\frac{a}{\lambda}$. Therefore, σ_{abs} is dominated for small sized particles, and σ_{sca} can not be ignored for large sized nanoparticles (note that $a \ll \lambda$). Additionally, the absorption and scattering peaks are highly sensitive to the medium. The resonance absorption (or scattering) will occur when $\varepsilon + 2\varepsilon_m \to 0$. From Drude mode with $\gamma \ll \omega$, the resonant frequency of spherical nanoparticles is derived.

$$\omega_{max} = \frac{\omega_p}{\sqrt{1 + 2\varepsilon_m}} \tag{1.28}$$

The resonant frequency is approximately linear with the refractive index (n), red-shifting and blue-shifting with increasing and decreasing the refractive index. For metal nanoparticles, the SPR are characterized by discrete, complex frequencies, depending on the size and shape of the object. LSPs are confined to curved metal particles. In contrast to the SPP mode that can be excited only if both the frequency and wave vector of the exciting light match the frequency and wave vector of the SPP, LSPs of nanoparticles with $d \ll \lambda$ can be resonantly excited with light of appropriate frequency irrespective of the wave vector of the exciting light, which is the well-known localized SPR. The resonant energy depends on the particle size and shape, and the permittivity (dielectric constant) of the metal nanoparticle itself and surrounding materials, and can be tuned by these factors. Different modes of localized SPR exhibit enhanced near-field amplitude at the resonance wavelength. This field is highly localized at the nanoparticle and decays rapidly away from the nanoparticle/dielectric interface into the dielectric background, though far-field scattering by the particle.

Therefore, with the adsorption or modification of molecular on the particle surface, the local medium environment changes or the particles will be assembled into a certain configuration, which will lead to the obvious shifting of resonant peak position [22]. Using this feature of SPR, scientists can realize highly sensitive biological and chemical sensors.

The localized SPR is the fundamental principle behind many technology applications. Another important characteristic of SP in application is quality factor (Q), which is the number of electron oscillations that occur coherently, and during which the mode is able to sustain its phase and accumulate energy from the external excitation field. The Q ($Q = \frac{\omega}{2\gamma}$) of plasmonic metals ranges from 10 to 100. The SP spectral width (or relaxation rate) γ, quality factor Q and lifetime of SP depends explicitly only on the optical frequency ω and the image part of permittivities of the metal. This lifetime is in the range 10–60 fs for silver and 1–10 fs for gold in the plasmonic region. These data show that nanoplasmonic phenomena are ultrafast (femtosecond) [2].

In response to an external excitation, a plasmonics nanoparticle can generate local fields that are enhanced by Q with respect to the external field. The region occupied by these enhanced fields is determined solely by the size of the nanoparticle. Another route to enhancing the local field is through adjusting the morphology. For instance,

the sharp tip can create intense local fields, which will be delivered in Chapters 4 and 7 for nanostructures based on the Au nanobipyramids.

The above LSP is a quasi electrostatic model, in which metal nanoparticles are treated as dipoles. The delay effect and radiation attenuation effect of electric field in particles are not considered in this model. And it can only be used to calculate particles with diameter much smaller than the wavelength. When the particle size large and comparable to the wavelength, electric field in the particle is no longer uniform because of the small penetration depth of electric field in particles, as discussed in Section 1.5.2. For this case, quadrupole and octupole must be considered, and the polarizability of large sized particle must modified according to the long wavelength approximation, as widely reported in many literatures. On the other extreme direction, influence of strong coupling effect and quantum tunneling effect on plasmons should be considered when the particle size is smaller than the critical size.

Since an LSP is confined to a particle (or a curved surface), it results in a significant electromagnetic field enhancement at small metallic particles due to the small volume of the LSP mode. This effect contributes to numerous phenomena such as light emission from STM tunnel junctions, enhanced scattering, surface enhanced Raman scattering, and second-harmonic generation, and finds applications in active photonic elements and apertureless scanning near-field microscopy.

1.6.4 Other Surface Plasmon Supports

Because of their large negative values of the real part of permittivity, metals are excellent materials for plasmonic applications, particularly noble metals of Au and Ag. These two materials have been used frequently in plasmonics due to their chemical stability and relatively low Ohmic loss in the Vis-NIR wavelength region. Other materials such as Na, Al, Ni, Pt as well as oxides and metallic alloys have demonstrated plasmonic properties.

Different from plasmon mode supported by the isotropic metal or heavily doped semiconductor surface [23], the plasmon in two-dimensional materials is confined to a plane, and its attenuation is greatly suppressed. As a typical two-dimensional material, graphene has become a very popular plasmon support. However, as a semi metal, plasmon frequency of graphene located in the infrared region due to its low carrier concentration. Other two-dimensional materials are also mostly semi-metallic (such as $TiSe_2$) or semi-conductive (such as BN and MoS_2) with low carrier concentration. Thus, it is urgent to find suitable two-dimensional metal materials for integrated photonics device. Bornene is a new two-dimensional material with intrinsic metallicity, and it can be a promising plasmon support with low attenuation.

As two dimensional materials with in-plane anisotropy, it is predicted to be the second kind of wail semi metal with series of novel electrical properties, such as ultra-high electron mobility and adjustable carrier concentration. Recently, two dimensional hyperbolic plasmon resonance mode in far infrared band was detected in the WTe_2 thin film through optimizing Fourier transform infrared spectroscopy [24].

1.6.5 Detection of Surface Plasmon

Localized SPR of metal nanoparticles were historically probed on UV-Vis-NIR spectrometer by illuminating the sample with far-field plane-wave light and studying the optical response by measuring absorption, scattering spectra. The spectra are an average effect of many particles dispersed in one sample. In 2001, Nagao et al. reported, for the first time, energy and the linewidth dispersion of a plasmon in a dense two-dimensional electron system on a silicon surface. The plasmon energy dispersion exhibited an excellent agreement with the nearly free-electron theory [25].

After SP excitation, it will decay according to two categories: radiative SP decay (studied seldom) and nonradiative SP decay in most cases. Nonradiative decay of SP is usually considered an unwanted process. Much effort was focused on avoiding or mitigating nonradiative SP decay. However, recent studies have proven that hot carriers generated from nonradiative SP decay can be used in many practical applications are plagued by the plasmonic loss – SP diphase, such as photothermal effect, surface imaging, and hot carrier photodetection [26].

Photodetection for the SP includes hot electron and hot hole photodetectors. Compared with hot hole (lower than Fermi level in d band) detection, hot electron (higher than Fermi level) detectors have been widely studied. For example, optical antenna can realize effectively photoelectric conversion and detection, in which the hot electrons in metal nanoantennas can be injected into adjacent semiconductors. However, nanoantennas are usually in subwavelength size, which often requires complex and expensive processing technology, such as electron beam exposure and focused ion beam etching. Another coupling structure of surface plasmon and low dimensional nanomaterials can also realize local electric field enhancement. The low dimensional nanomaterials, such as nanowires, quantum dots, and two-dimensional materials, act as excellent thermionic acceptor and can be applied to construct plasmon hot electron detectors.

Since the plasmons can be excited by both photons and electrons, they can also be detected by means of electrons. In 1957, the existence of surface plasmons in a thin metal film was theoretically predicted by Ritchie [27] for electron energy losses in thin metal film below the bulk plasmons and soon experimentally demonstrated in 1959 by Powell [28]. Stern and Ferrell, in 1960, used transmission experiments to probe the dispersion of the electron energy loss as a function of scattering angle [29]. The experimental observation of LSPRs in metal spheres excited by 50 keV electrons was reported in later of 1960s [30].

With the emergence of energy-filtered TEM and spectrum-image mode in the STEM in the 1980s of metallic nanoparticles, the SP modes and charge distribution were well characterized. Oftentimes, one particular energy is selected for examination and the spectral intensity is plotted as a function of position, resulting in an energy-filtered spectrum-image, which is commonly known as an electron energy loss spectroscopy (EELS) map. The early EELS experiments was the first observation of the bulk plasmon in thin Al film [31]. However, the early EELS experiments were not able to reveal the spatial profiles of LSPR, and it was not until the emergence of the energy-filtered TEM and STEM in the 1990s that mapping

studies became possible typically for high-energy atomic transitions beyond the visible region (400–700 nm). The first EELS mapping experiments represented a significant step toward SPR mapping were reported by Nelayah et al., in 2007 [32]. In their work, mappings the localized SPR modes in Au and Ag nanostructures down to region of 1.75–3 eV.

EELS performed in an STEM has demonstrated unprecedented power in the characterization of surface plasmons. For example, Song et al. investigated the plasmon excitation in individual Ag nanoparticles and plasmon maps of coupled Ag nanoparticles [33]. They found that the intensity maxima are distributed along the circular edge of the particle, where the electron beam excites the plasmon effectively. The line profile of the plasmon intensities is shown in Figure 1.10a.

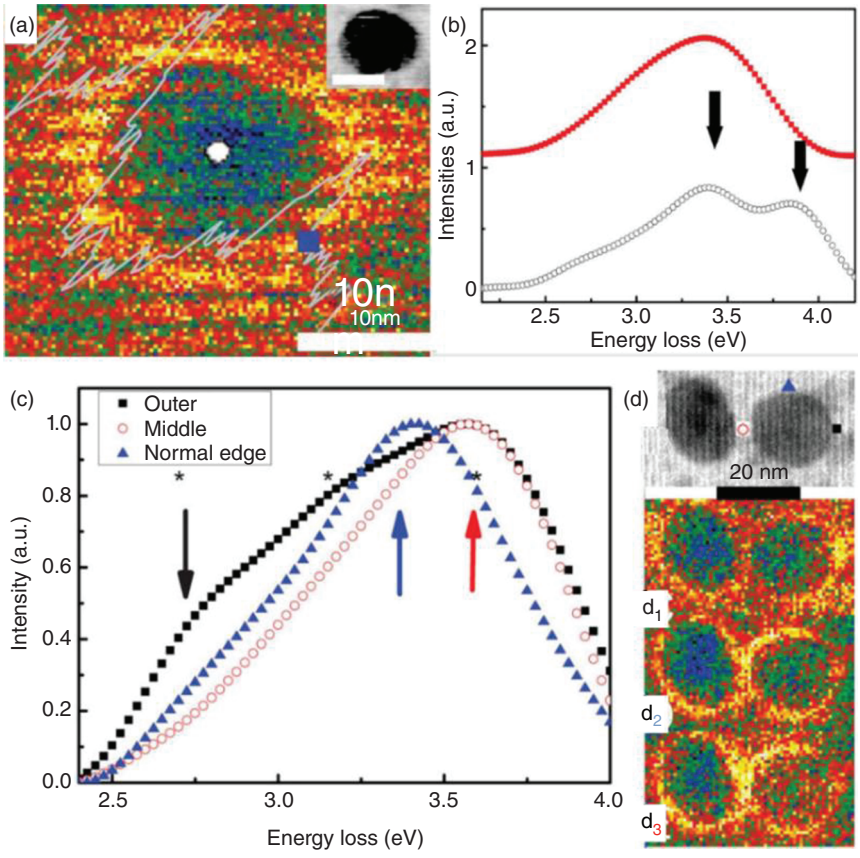

Figure 1.10 (a) EEL intensity mapping of an Ag particle (energy window: 3.3–3.6 eV). The gray curve is the line profile and the top right is the STEM image. The two spots mark the extraction positions of the EEL spectra in (b). EEL spectra from the spots in (a). The top curve is from the white-circle spot and the bottom curve is from the blue-box spot. (c) EELS from the spots marked in the STEM image of (d), where the red-circle, black-box, and blue-triangle curves refer to the middle, outer edge, and perpendicular edge of the cluster dimer, respectively. The black asterisks mark three features of the spectrum from the black spot. Source: Song et al. [33]/Reproduced with permission from ©2010, JOHN WILEY & SONS, INC.

The maximum in plasmon intensity in the spectrum is located at 3.4 eV, which is assigned to the spherical mode of Ag nanoparticles. When the electron beam is in the middle of the nanoparticle, another feature emerges at 3.8 eV due to the interband transition of the bulk Ag, as shown in Figure 1.10b. For a given dimer with two identical spheres, the EELS extracted from the spots turned out as expected and are shown in Figure 1.10c,d. The distinct spectra from three regions, as shown by the spots in Figure 1.10d, that is, the edge parallel to the center axis (blue triangles), the edge perpendicular to the axis (black boxes), and the center (red circles). The maximum intensities of EELS in Figure 1.10d1–d_3 fall around the black, blue, and red spots, respectively, corresponding to the EELS mappings with energy windows of (d_1) 2.6–2.9, (d_2) 3.2–3.5, and (d_3) 3.5–3.8 eV. And they assigned the in-phase mode at 2.7–2.9 eV and the anti-phase mode at 3.6 eV. These positions agree with those predicted theoretically.

Nowadays, the subangstrom spatial resolution achieved in EELS and its capability of exciting the full set of LSPR modes supported by a metallic nanostructure makes STEM/EELS an ideal tool in the study of LSPR. The plasmonic properties characterized using EELS can be associated with geometric or structural features collected simultaneously in a STEM to achieve a deeper understanding of the plasmonic response.

1.7 Surface Plasmon Effects

Under excitation, SP can either propagate on a planar metallic surface as SPP or be confined to the particles known as LSP, providing a novel means of enhancing light-matter interaction at the nanoscale. Especially for the LSP of metal nanostructures, it has the characteristics or advantages of selective light scattering and absorption, electric field localization and strong enhancement. More and more achievements show that surface plasmons are promising in the fields of biology, chemistry, materials, energy, catalysis, and so on. Here, we present some typical surface plasmon effects, such as field enhancement and hot electron effect that are of great important for catalytic reaction, surface enhanced spectroscopy, photothermal conversion and photoelectric device.

1.7.1 Electric Field Enhancement

Surface plasmons are oscillations confined to the surfaces of conducting materials and interact strongly with light. It is well-known that a metal particle of Au or Ag having an intense localized surface plasmon resonance (LSPR) peak can act as a nanoantenna for trapping light to form a locally enhanced electric field in the proximity of metal nanoparticles. After surface plasmon excitation, resonant energy transfer is a nonradiative energy transfer process. Based on the energy transfer mechanism, light-harvesting structures have been designed to implement the performance of detectors or photovoltaic structures [34].

Irradiating metal nanoparticles with light at their plasmon frequency generates intense local electric fields at the surface of the nanoparticles. Electromagnetic

simulations using the FDTD method have shown that the electric field intensity of local plasmonic "hot spots" can reach as much as 1000 times that of the incident electric field [35]. In these "hot spot" regions, the electron-hole pair generation rate is 1000 times that of the incident electromagnetic field. When the metal nanoparticles were coated on the surface of semiconductor, such as the commonly applied TiO_2 and CdS, photo-induced charge is generated locally in the semiconductors due to the local near-field enhancement of nanoparticles LSPR effect. Torimoto et al. found that the LSPR-induced electric field and photocatalytic activity of $Au/SiO_2/CdS$ for photocatalytic H_2O splitting greatly depend on the distance between CdS and Au nanoparticles, which further supports the near-field electromagnetic enhancement mechanism [36]. It is found that direct deposition of Au on CdS photocatalysts is not suitable for the photocatalytic H_2O splitting due to the direct photoinduced electron transferring from CdS to Au particles. At the same time, simple particle mixture of $CdS@SiO_2$ and $Au@SiO_2$ did not cause any enhancement of H_2 evolution rate because the intensity of the LSPR-induced electric field decays with increase in distance from the metal surface. Therefore, photocatalysts of semiconductor nanoparticles are expected to be effectively photoexcited only when the distance between metal and semiconductor nanoparticles is appropriately adjusted.

Ho et al. investigated the plasmonic response of Au/TiO_2-dumbbell-on-Au-film nanocavities and explore the physical mechanism of dumbbell-film coupling mediated hot-carrier generation and transfer at the two TiO_2-Au interfaces, as shown in Figure 1.11 [37]. From Figure 1.11a, hot carriers can be generated only through localized SPR excitation in the Au NR in the $Au/TiO_2/ITO$ system. However, both localized SPR excitation in the Au NR and direct optical excitation of d-band transitions in the Au film can induce hot carriers in the $Au/TiO_2/Au$ system. The dual-channel carrier generation mechanism associated with the $Au/TiO_2/Au$ system leads to an intriguing carrier transport process, as illustrated in Figure 1.11b. FDTD Solutions was applied to investigate their extinction response and electric near-field distribution profile of the longitudinal and transverse resonance modes for the two systems, as displayed in Figure 1.11c,d. Compared to the Au/TiO_2 dumbbell on the ITO substrate, the longitudinal localized SPR of the Au-film-coupled nanocavity exhibits a linewidth shrinking. Moreover, the extinction intensity of the two resonance modes in the Au-film-coupled nanocavities is obviously enhanced compared to that for the Au/TiO_2 dumbbells on ITO, which is originated from the plasmonic coupling between the Au/TiO_2 dumbbell and the Au film. They found that Au/TiO_2 dumbbell nanostructures assembled on a thin Au film serve as an efficient optical absorber and a hot-carrier generator in the visible region. Upon excitation of LSPs in such coupled particle-on-film nanocavities, the energetic conduction electrons in Au can be injected over the Au/TiO_2 Schottky barrier and migrated to TiO_2, participating in the chemical reaction occurring at the TiO_2 surface.

Plasmonic enhancement has also been demonstrated in photocatalytic methane formation by the reduction of CO_2 with H_2O. Usually, photocatalytic CO_2 reduction is a more challenging problem than solar water splitting due to its requirement of conduction band edge, additional photovoltage, and multielectron process. Similar work was carried out by Hou et al. They found the quantum efficiency to be greatly

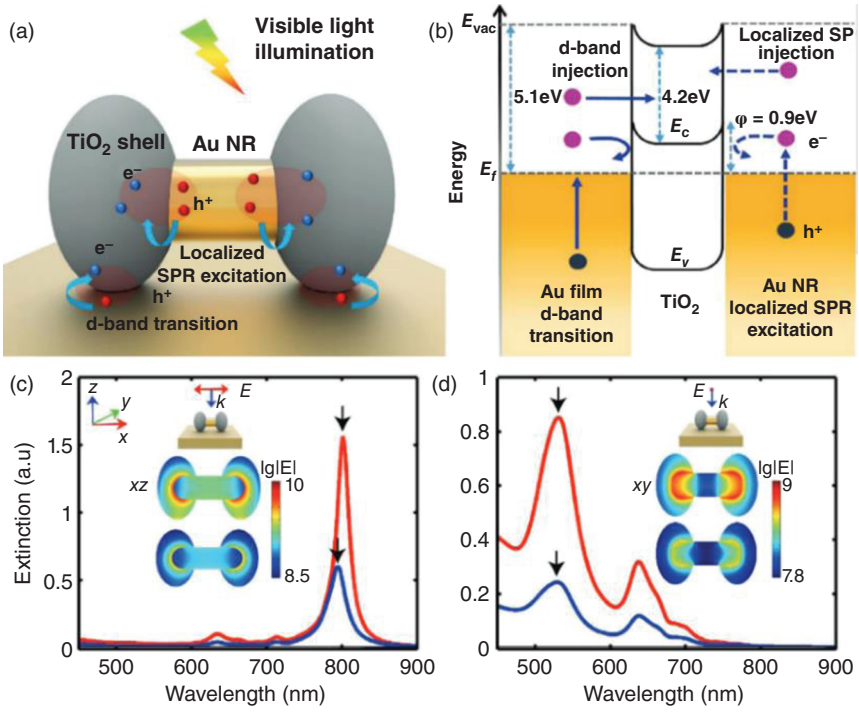

Figure 1.11 (a) Pictorial sketch of the hot-carrier generation in an Au/TiO_2-dumbbell-on-Au-film nanocavity through both localized SPR excitation and d-band transitions. (b) Schematic band diagram for an Au/TiO_2-dumbbell-on-Au-film nanocavity, illustrating the pathways of hot-carrier excitation and injection. The work function of Au, and affinity of TiO_2 are indicated in the band diagram. Simulated extinction spectra of an Au/TiO_2 dumbbell nanoparticle with experimentally determined geometrical dimensions on a 100 nm thick Au film (red lines) and on a semi-infinite ITO substrate (blue lines): (c) the incident E-field is parallel to the x-axis and (d) parallel to the y-axis both under normal incidence. Each inset shows corresponding excitation configuration and simulated electric near-field distribution profiles at the resonance wavelengths as labeled by the arrows. Source: Reproduced from Ho et al. [37]/with permission of John Wiley & Sons.

improved by integrating Au nanoparticles with TiO_2 when the photon energy (532 nm) matches the plasmon resonance of the Au nanoparticles [38]. To obtain a more rigorous understanding of the mechanism of catalytic enhancement, they performed numerical simulations of the charge and electric potential distributions at the Au nanoparticle-TiO_2 interface under plasmon resonance excitation. The electromagnetic response of the film was dominated by local hot spots where the electric field intensity reaches 1000 times that of the incident electric field at the TiO_2 surface. They also found that the plasmon-excited electrons in the Au nanoparticles cannot transfer directly from the Au to the TiO_2. Only when the photon energy is high enough to excite the d band electrons of Au to a conduction band that lies above the conduction band of TiO_2, does direct charge transfer occur between these two materials. When the incident photon energy is high enough (254 nm in UV region), an additional mechanism involving the interband electric

transitions in Au produces a number of additional photocatalytic reaction products. In this wavelength range, both the excited electrons in Au and TiO_2 contribute to the reduction of CO_2 with H_2O vapor.

In recent years, CO_2 methanation via heterogeneous catalysts has attracted a considerable attention. Significant progress has been made in this direction, as expressed by Figure 1.12a in a review paper of Aziz et al. [39]. For example, Fu et al. designed wide-spectrum sunlight-driven Rh/Al nanoantenna as photothermal catalyst [40]. The detailed results verified that the CO_2 methanation process was facilitated by the localized SPR and nanoantenna effects of the Rh/Al nanostructure under light irradiation, as illustrated in Figure 1.12b–d. Combined with the photocatalytic oxidation for H_2 generation and catalytic reduction of CO_2, it is expected that these work could bring more insights and inspirations for solar-driven catalysis toward clean and sustainable fuel conversion.

Now, "hot spots" created around the plasmonic nanostructures can greatly promote the interaction between light and matter, enabling efficient excitation of molecules. Conversely spectral information about molecules in the hot spots can be broadcasted to the far field. This process is accompanied by the enhancement of light absorption radiation scattering light force resonance migration and photo-thermal effects. The rich phenomena associated with LSP nanostructures resulted in the application of surface enhanced Raman spectroscopy (SERS) and tip enhanced Raman spectroscopy (TERS), which provides "fingerprints" for

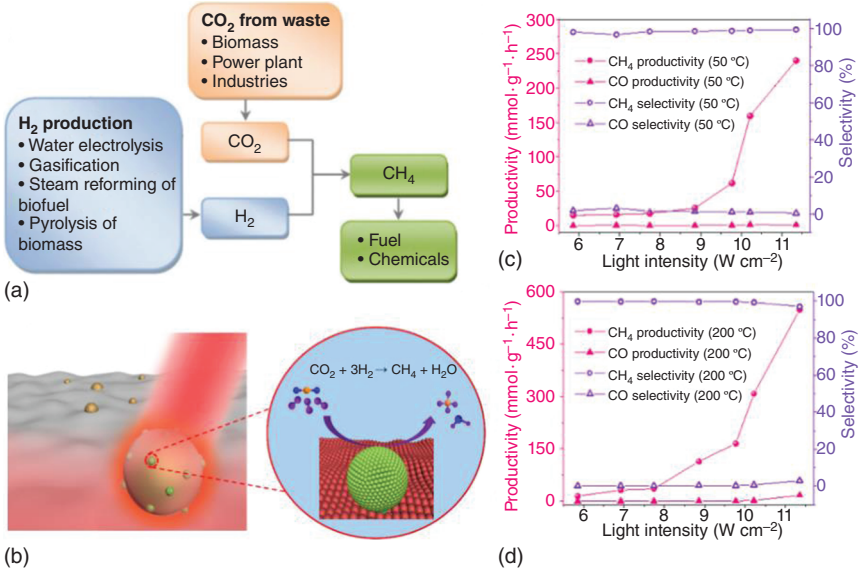

Figure 1.12 (a) Overview of CO_2 methanation. Source: Adapted from Aziz et al. [39]. (b) Schematic diagrams of photothermal CO_2 methanation on the Rh/Al nanoantenna catalyst. CH_4 and CO productivity and selectivity under different simulated sunlight intensities at the chamber temperatures of (c) 50 and (d) 200 °C. Source: Reproduced from Fu et al. [40]/with permission of American Chemical Society.

recognizing chemical species in neighboring surfaces, making it a promising tool for in-situ observation of catalytic process [41–47].

In addition to the tunable absorption/scattering, large extinction cross section and local field enhancement effect metal nanostructures, the LSP resonant position is highly dependent on the medium, size and shape of the nanostructure. With the adsorption or modification of molecular on the particle surface, the local medium environment changes or the particles will be assembled into a certain configuration. These changes will lead to the obvious shifting of resonant wavelength of plasmonic nanostructure. This feature enables metal nanostructures to be promising for the rapid sensing and detection of chemical and biological objects [48, 49]. With the epidemic outbreak of global Novel Coronavirus 2019 (abbreviated as 2019-ncov), the State Food and Drug Administration approved the novel coronavirus antibody detection reagent.

1.7.2 Hot Electrons Effect

In metals with high concentration of free electrons, the proportion of radiation recombination in metal microstructure is very weak, which is quite different from the excitation and radiation recombination of semiconductor. When the incident light on the nanostructure is resonant with LSP, the photon energy drives the surface of plasmon to produce collective oscillation within 10 fs, during which the electrons energy is higher than the Fermi level and becomes high-energy electrons. In the following 100 fs, the internal damping effects, such as phonon scattering, lattice defects and Landau damping, lead to excitation dephasing to produce electron hole pairs. Through the scattering between electrons and optical phonons, the energy of electrons is finally transferred to phonon vibration energy after excitation (~1 ps). Then the phonons energy is transformed into the heat energy of lattice vibration (~10 ps), generating localized heat on the nanometer sized region. The localized energy dissipated into the environmental medium through the process of heat radiation and heat conduction after ~1000 ps. The mechanism and energy conversion process is presented by Figure 1.13 [50]. The photothermal conversion can be regulated and localized in a nanogap or nanometer sized cavity. Each stage of these energy transfer processes can be used for a specific application. Many research papers and some review articles have dealt with the plasmon related applications [51–53].

1.7.2.1 For New Energy

Under optical excitation, plasmon quantum can decay either radiatively into a photon or nonradiatively into an electron-hole pair. The most likely electron-hole pair formation occurs when the plasmon quantum excites an electron from the Fermi level to an occupied state below the vacuum level. These hot electrons can transfer into specific electronic states of molecules adsorbed on the metal surface, inducing processes such as molecular dissociation and chemical reactions.

Mukherjee et al. [54] reported experimental evidence of room temperature photocatalytic dissociation of H_2. The reaction can only be enabled by hot electrons

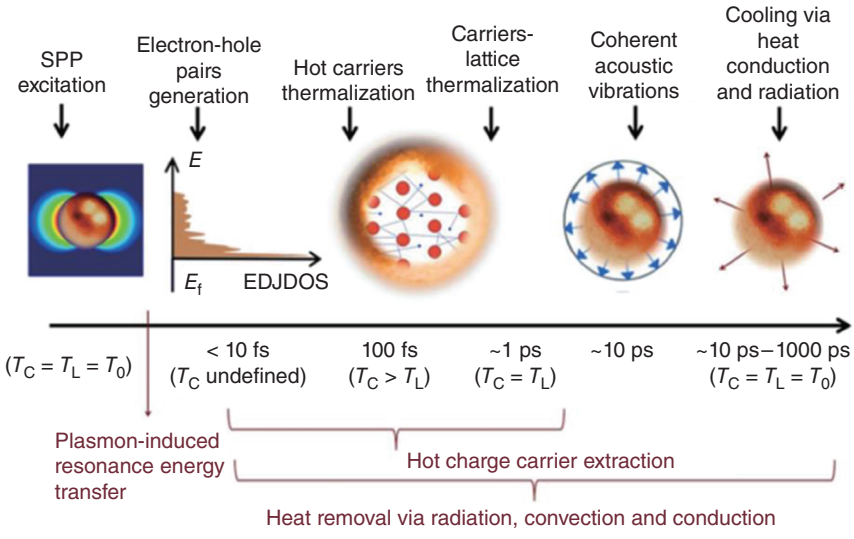

Figure 1.13 The timescales and mechanism and energy conversion process of LSP after irradiation. Source: Reproduced from Boriskina et al. [50]/with permission of Chinese Laser Press.

generated by surface plasmon decay from small Au nanoparticles supported on TiO_2 matrix. The dissociation of H_2 process was probed by detecting the formation of HD molecules from the dissociations of H_2 and D_2. The photocatalysis was confirmed with and without laser illumination. They also observed a steady increase of photocatalytic rate with increasing Au loading, showing a strong dependence on Au nanoparticle concentration for HD generation. As shown in Figure 1.14, the hot electrons are initially optically excited at the Au nanoparticle surface. Then hot electrons soon lose coherence and form a nonequilibrium Fermi-Dirac type distribution which thermalizes by Auger scattering. The narrow bonding and broad antibonding states of adsorbed H_2 are denoted as B and AB, respectively. The hot electrons in the high energy tail of this distribution have sufficient energy to transfer into the antibonding state of the H_2 molecule, creating a transient negative ion. Then the transient negative ion transfers the electron back to the AuNP surface, where it returns to the ground-state potential energy continuum and dissociates.

Although silicon or metal oxides are still under development for solar energy devices. These materials cannot meet the requirements for practical applications due to one or more shortcomings, such as large bandgap, low absorption of solar radiation, low charge mobility, high-density surface trap states, and indirect bandgap feature. To extend the light absorption spectral range and to improve the energy conversion efficiency of semiconductors, plasmonic metal nanostructures with broad absorption are incorporated to form metal-semiconductor Schottky junction. Plasmonic hot electrons can enter semiconductor across the Schottky junction or through the Schottky emission. Through introduction of an ultrathin passivate insulator or organic interface, the power conversion efficiency were greatly improved.

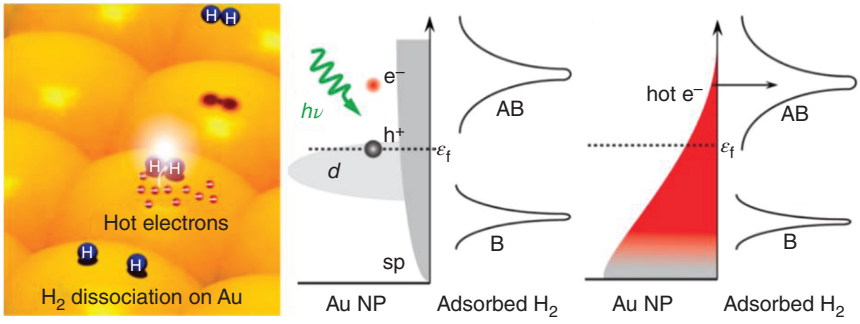

Figure 1.14 (a) Mechanistic representation of H_2 dissociation on the Au nanoparticle surface. (b) Schematic of hot electron excitation in Au nanoparticle showing: d-band electron-hole pair excited above the Fermi level upon plasmon decay. The narrow bonding and broad antibonding states of adsorbed H_2 are denoted as B and AB, respectively. (c) Schematic of Fermi-Dirac type distribution of hot electrons permitting hot electron transfer into the antibonding state of H_2. Source: Mukherjee et al. [54]/Reproduced with permission from © 2013, American Chemical Society.

One potential of the hot electrons effect of LSP is the solar photothermal conversion. Due to the unique optical absorption and thermal localization characteristics of plasmon absorber, researchers have greatly improved the efficiency of solar energy generation through material selection, structural design and system optimization. It is expected that solar photothermal effect can be widely used in the fields of seawater desalination, sewage treatment, high-temperature steam sterilization, and power generation. At the same time, some scientific problems, such as the photothermal conversion mechanism of thermal and dynamic processes and the precise control of thermal effects in time and space, can be solved with the development of ultrafast spectroscopy technology.

Most recently, due to unique capability of broadband light harvesting and pronounced electromagnetic field enhancement, plasmonic nanostructures have been demonstrated for promising applications in a new sustainable field of plasmon enhanced water purification. Chen et al. [55] demonstrated Ag-based asymmetric plasmonic structure for dual functions of solar water purification and pollution detection, as shown in Figure 1.15. Such impressive performance in solar thermal conversion and chemical sensing are stemmed from the broadband and efficient light absorption (solar absorptivity > 90%) as well as pronounced local field enhancement, respectively. As an example of functional integration, this dual functional Ag-based plasmonic structure can enable on-site pollution detection and purification of water.

The concept of complex plasmonic structures based on Au and Ag nanostructures with integrated functionalities opened up exciting opportunities for advanced plasmonic science [56]. In 2016, through physical vapor deposition and assembly of Au nanoparticles in the Al_2O_3 template, Zhou et al. achieved plasmon absorber with high efficiency in the ultra-wide band range of 400 nm to 10 μm [57]. Through depositing Pb, Au, Ag particles mixture evenly into the pores of natural wood, Zhu

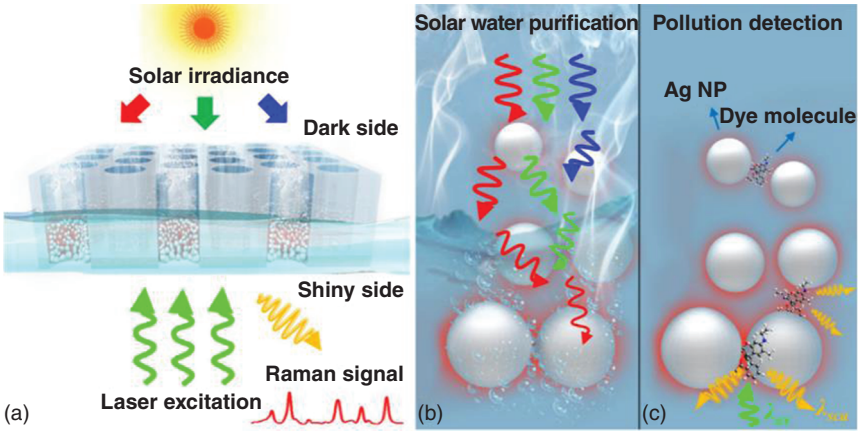

Figure 1.15 Schematic of the integrated dual-functions of an Ag-based plasmonic structure: Plasmonic heating and spectroscopic amplification. (a) The schematic of structure, the dark side (facing up toward the light) for the solar water purification and the shiny side (facing down toward the laser illumination) for the pollution detection. (b) Mechanism for the dark side of the structure enabled solar water purification. (c) Mechanisms for the shiny side of the structure enabled organic pollution detection. Source: Chen et al. [55]/Reproduced with permission from ©2018, ELSEVIER.

obtained plasmonic wood absorbers with excellent performance of solar steam generation [58].

1.7.2.2 For Photoelectric Device

Another important application of hot electron effect of LSP is enhancement or tunability in photoelectric device. Metal nanostructures generate "hot electrons" from light by creating surface plasmons [59]. There are several proposed metal-to-semiconductor charge-separation pathways. Based on the conventional plasmon-induced hot-electron transfer (PHET) mechanism (Figure 1.16a), the reported efficiencies of devices based on this PHET concept are often low (1–2%) because the plasmon decays into a hot electron-hole pair within the metal via Landau damping on time scales of a few to tens of femtoseconds. Hot-electron transfer competes with electron relaxation through rapid electron-electron scattering on time scales of hundreds of femtoseconds [60, 61]. Metal-to-semiconductor hot-electron transfer efficiencies can be enhanced if the competition with ultrafast electron-electron scattering in the metal can be avoided. One approach is to create a direct metal-to-semiconductor interfacial charge-transfer transition (DICTT) that can be directly excited to promote an electron from the metal into the semiconductor CB. However, these interfacial transitions are often too weak as compared with bulk metal transitions [60]. A desirable photoinduced hot-electron transfer pathway would combine the strong light-absorbing power of plasmonic transitions with the superior charge-separation.

In 2015, Wu et al. first proposed and experimentally demonstrated a plasmon-induced metal-to-semiconductor interfacial charge-transfer transition (PICTT)

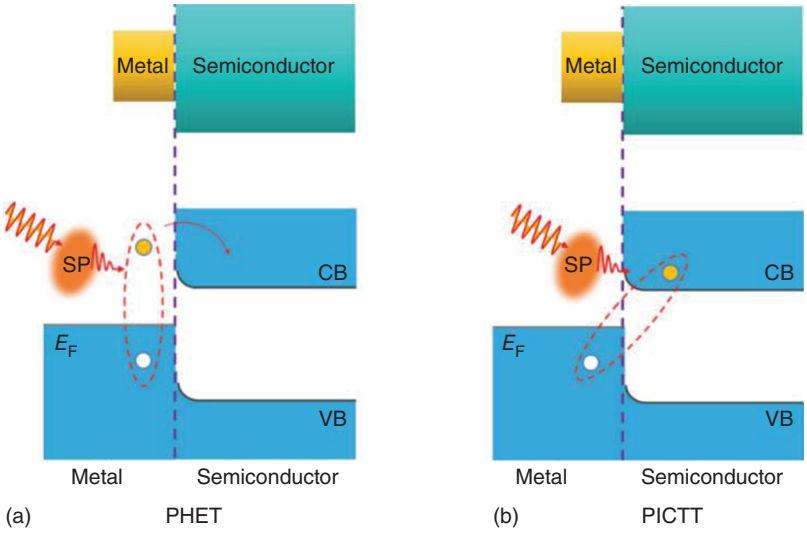

Figure 1.16 Metal-to-semiconductor charge-separation pathways. (a) Conventional PHET mechanism, in which a photoexcited plasmon in the metal decays into a hot electron-hole pair (solid and open red circles in the dotted ellipsoids) through Landau damping, followed by injection of the hot electron into the CB of the semiconductor. (b) The PICTT pathway, in which the plasmon decays by directly generating an electron in the conduction band of the semiconductor and a hole in the metal. VB is the semiconductor valence band and hv indicates the excitation photons. Source: Zhu et al. [26]/with permission of AIP Publishing LLC.

pathway in CdSe-Au NR heterostructure, as presented in Figure 1.16b [62]. In this PICCT pathway, strong Au–CdSe interactions led to strong plasmon damping in the Au tip. When the plasmon was excited along the nanorods axis, transient absorption anisotropy showed more efficient (>24%) charge transferred from Au to CdSe, and the charge-separation efficiencies were independent of excitation photon energy. The damped plasmon decays via direct excitation of an interfacial electron-hole pair (with an electron in CdSe and a hole in Au). The electronic structure of CdSe–Au NRs can be viewed as a combination of the strongly interacting tip region, which resembles the CdSe-Au dimers with strongly damped plasmon and exciton bands. The center part is similar to the unperturbed CdSe nanorods. Direct evidence to support this proposed mechanism was obtained through ultrafast transient absorption study. A pump laser with a photon energy below the CdSe band gap was used to excite the Au tip, and the electron transferred to the CdSe domain was probed through the bleaching of the exciton.

1.7.2.3 For Plasmonic Nanolaser

The plasmonic nanolaser (also called SPASER abbreviated for "surface plasmon amplification by stimulated emission of radiation") is an active nanosystem including a gain medium and a plasmonic metal nanoparticle core. It theoretically predicted in 2003 by Bergman and Stockman from Georgia State University [63]. Then kinds of surface plasmon nanolasers with new structures have been

constructed. Nanolasers applied the idea of SPP effect that can break through the diffraction limit. Researches of nanolaser were focused on minimizing metal loss and realization of electric pump at room temperature and low threshold.

Nanolasers based on surface plasmon are not pumping and feedback of optical resonators in optical systems. Under the irradiation of electromagnetic wave, the stimulated oscillation of free electrons can produce strong LSPR on the nanometer scale. The oscillation in the resonant cavity was amplified by the gain medium and laser emission can be achieved [64].

In 2008, Oulton et al. proposed a novel scheme and designed a waveguide structure composed of semiconductor-insulator-metal (SIM) for F-P mode laser operation [65]. The gain medium of the laser is semiconductor nanowires. And the photons generated by nanowires are coupled with free electrons on the metal surface to form surface plasmon. The plasmon propagates along the direction of the nanowire and oscillates in the Fabry-Perot cavity formed by reflection at both ends of the nanowire. In 2009, Zhang et al. verified the design feasibility in experiments and prepared nanowire surface plasmon nanolaser [66]. Then different nanolasers of plate or multilayer structures were prepared, such as metal–semiconductor–metal (MSM), MIM, metal–oxide–semiconductor (MOS), as summarized by Ma et al. [67]. In their review paper, the plasmonic confinement effect on the plasmon laser through the enhancement of spontaneous emission in sub-wavelength-scale plasmonic cavities, ultrafast behavior of plasmon laser, as well as future prospects and challenges were discussed.

In 2014, Lu et al. reported broadband tunable, single-mode plasmonic nanolasers, based on a single MOS nanostructure platform comprising of InGaN/GaN semiconductor nanorods supported on an Al_2O_3-capped epitaxial Ag film [68]. They successfully reduced the continuous-wave lasing thresholds to ultrasmall values for all three primary RGB colors and possibility of "thresholdless" lasing operated at 7 K for the blue plasmonic nanolaser. Although the lasing line width is not in the lasing region as predicted by the classical Schawlow-Townes theory, temperature evolution of the spectral for the device with plasmonic cavity indicated the line width is in the lasing regime. Photon bunching is characteristic of the spontaneous emission of the gain medium. And the line width alone is not be a conclusive indication of lasing.

This new type lasers can not only greatly reduce the energy loss in metal, but also realize long-distance surface plasmon wave transmission. At the same time, the threshold of laser is reduced, which makes it possible for the nano laser work at room temperature. Once the nanolaser with low threshold and high integration is successfully developed, the size of photonics devices will be greatly reduced. Thus, the mismatch between photonic devices and electronic devices will be improved, and the product size in the optoelectronic industry will be reduced. Nanolaser with high performance will be great useful in biosensors, precision measurement and so on. Among the potentials of nanolaser, the "killer" application will be ultrafast, high-density on-chip communications for future information processing. Some of our recent work about plasmon enhanced photoelectric devices, including plasmonic nanolaser with single mode, can be seen in Chapter 9.

1.8 Summary of this Chapter

In this chapter, we present the theoretical backgrounds and research advances of plasmonics, including plasmon originated from the collective oscillation of free electron based on Drude mode, SPPs at metal-vacuum interface, propagation characteristic of SPP. Then advances in the electric and optical excitation and detection of SPP, as well as the LSP of nanostructures were delivered. Rapid development in synthesis and fabrication techniques resulted in the availability of systematically designed plasmonic materials and devices, which not only widened the scope of applications of plasmon and hot carriers but also advanced experimental discoveries.

In recent years, surface plasmon effects, such as energy transfer, hot electron transfer, and field enhancement effect, can be used to enhance photocatalysis and realize plasmon capture light energy. Although there are many hot topics in the plasmon related fields, the internal physical mechanism remains to be revealed. More researches were limited on the plasmonic metals of Au, Ag, Cu, and Al, as well as some two dimensional materials, working on certain bands with own advantages and limitations. It is found that heavily doped semiconductors can also generate hot carriers by themselves with more high energy transfer efficiency due to less energy loss via the indirect transfer pathway across the interface or via the direct transfer pathway with easier orbital hybridization. Plasmonic semiconductor nanostructures are promising candidates that can manifest SPR under visible-light or infrared-light excitation. Moreover, they have been used for SERS, photocatalysis, and water splitting.

However, fully understanding the enhancement effect of plasmon and its internal physical process can effectively promote the application, especially for the coupling structures with controllable energy exchange and transfer path. Among these issues, some related works should be developed simultaneously, such as theoretical models and calculation methods, design and preparation, characterization and testing, ultrafast time resolution and high resolution space detection technology.

References

1 Pines, D. and Bohm, D. (1952). A collective description of electron interactions: II. Collective vs individual particle aspects of the interactions. *Phys. Rev.* 85: 338.

2 Stockman, M.I. (2011). Nanoplasmonics: past, present, and glimpse into future. *Opt. Express* 19 (22): 22029–22106.

3 Bohren, C.F. and Huffman, D.R. (1983). *Absorption and Scattering of Light by Small Particles*. Wiley.

4 Drude, P. (1900). Zur Elektronentheorie der Metalle. *Ann. Phys.* 1: 566–613.

5 Johnson, P.B. and Christy, R.W. (1972). Optical constants of noble metals. *Phys. Rev. B* 6: 4370–4379.

6 Blackstock, A.W., Ritchie, R.H., and Birkhoff, R.D. (1955). Mean free path for discrete electron energy losses in metallic foils. *Phys. Rev.* 100: 1078.

7 Xu, M.S., Liang, T., Shi, M.M., and Chen, H.Z. (2013). Graphene-like two dimensional materials. *Chem. Rev.* 113: 3766–3798.

8 Falk, A.L., Koppens, F.H.L., Yu, C.L. et al. (2009). Near-field electrical detection of optical plasmons and single-plasmon sources. *Nat. Phys.* 5: 475–479.

9 Zayatsa, A.V., Smolyaninov, I.I., and Maradudin, A. (2005). Nano-optics of surface plasmon polaritons. *Phys. Rep.* 408: 131–314.

10 Zhou, Y.J. and Eda, G. (2017). Efficient carrier-to-exciton conversion in field emission tunnel diodes based on MIS-type van der Waals heterostack. *Nano Lett.* 17: 5156–5162.

11 Palash, B., Alexandre, B., and Lukas, N. (2011). Electrical excitation of surface plasmons. *Phys. Rev. Lett.* 106: 226802.

12 Ma, R.M., Oulton, R.F., Sorger, V.J. et al. (2011). Room-temperature sub-diffraction-limited plasmon laser by total internal reflection. *Nat. Mater.* 10: 110–113.

13 Kojori, H.S., Yun, J.H., Paik, Y. et al. (2016). Plasmon field effect transistor for plasmon to electric conversion and amplification. *Nano Lett.* 16: 250–254.

14 Fan, P., Colombo, C., Huang, K.C.Y. et al. (2012). An electrically-driven GaAs nanowire surface plasmon source. *Nano Lett.* 12: 4943–4947.

15 Yang, X., Ni, P.N., Jing, P.T. et al. (2019). Room temperature electrically driven ultraviolet plasmonic lasers. *Adv. Opt. Mater.* 7: 1801681.

16 Neutens, P., Lagae, L., Borghs, G., and Van Dorpe, P. (2010). Electrical excitation of confined surface plasmon polaritons in metallic slot waveguides. *Nano Lett.* 10: 1429–1432.

17 Sun, Z.P., Jiang, M.M., Mao, W.Q. et al. (2020). Nonequilibrium hot-electron-induced wavelength tunable incandescent-type light sources. *Photonics Res.* 8: 91–102.

18 Chu, M.W., Myroshnychenko, V., Chen, C.H. et al. (2009). Probing bright and dark surface-plasmon modes in individual and coupled noble metal nanoparticles using an electron beam. *Nano Lett.* 9: 399–404.

19 Mie, G. (1908). Beiträge zur optik trüber medien, Speziell kolloidaler metallösungen. *Ann. Phys.* 330 (3): 377–445.

20 Lorenz, L. (1898). *Sur La lumière réfléchie Et réfractée par Une sphère (Surface) Transparente*. Tome Premier, 403–529. Copenhague: libraire lehmanń & stage.

21 Debye, P. (1909). Der Lichtdruck Auf Kugeln Von Beliebigem Material. *Ann. Phys.* 335: 57–136.

22 Halas, N.J., Lal, S., Chang, W.S. et al. (2011). Plasmons in strongly coupled metallic nanostructures. *Chem. Rev.* 111: 3913–3961.

23 Agrawal, A., Cho, S.H., Zandi, O. et al. (2018). Localized surface plasmon resonance in semiconductor nanocrystals. *Chem. Rev.* 118: 3121–3207.

24 Wang, C., Huang, S., Xing, Q. et al. (2020). Van der Waals thin films of WTe_2 for natural hyperbolic plasmonic surfaces. *Nat. Commun.* 11: 1158.

25 Nagao, T., Hildebrandt, T., Henzler, M., and Hasegawa, S. (2001). Dispersion and damping of a two-dimensional plasmon in a metallic surface-state band. *Phys. Rev. Lett.* 86 (25): 5747.

26 Zhu, Y., Xu, H.X., Yu, P., and Wang, Z.M. (2021). Engineering plasmonic hot carrier dynamics toward efficient photodetection. *Appl. Phys. Rev.* 8: 021305.

27 Ritchie, R.H. (1957). Plasma losses by fast electrons in thin films. *Phys. Rev.* 106: 874–881.

28 Powell, C.J. and Swan, J.B. (1959). Origin of the characteristic electron energy losses in aluminum. *Phys. Rev.* 115: 869–875.

29 Stern, E.A. and Ferrell, R.A. (1960). Surface plasma oscillations of a degenerate electron gas. *Phys. Rev.* 120: 130–136.

30 Fujimoto, F. and Komaki, K.I. (1968). Plasma oscillations excited by a fast electron in metallic particle. *J. Phys. Soc. Jpn.* 25: 1679–1687.

31 Pettit, R.B., Silcox, J., and Vincent, R. (1975). Measurement of surface plasmon dispersion in oxidized aluminum films. *Phys. Rev. B* 11: 3116–3123.

32 Nelayah, J., Kociak, M., Stephan, O. et al. (2007). Mapping surface plasmons on a single metallic nanoparticle. *Nat. Phys.* 3: 348–353.

33 Song, F., Wang, T., Wang, X. et al. (2010). Visualizing plasmon coupling in closely spaced chains of Ag nanoparticles by electron energy-loss spectroscopy. *Small* 6 (3): 446–451.

34 Lunz, M., Gerard, V.A., Gunko, Y.K. et al. (2011). Surface plasmon enhanced energy transfer between donor and acceptor CdTe nanocrystal quantum dot monolayers. *Nano Lett.* 11 (8): 3341–3345.

35 Le, F., Brandl, D.W., Urzhumov, Y.A. et al. (2008). Metallic nanoparticle arrays: a common substrate for both surface-enhanced Raman scattering and surface-enhanced infrared absorption. *ACS Nano* 2: 707–718.

36 Torimoto, T., Horibe, H., Kameyama, T. et al. (2011). Plasmon-enhanced photocatalytic activity of cadmium sulfide nanoparticle immobilized on silica-coated gold particles. *J. Phys. Chem. Lett.* 2: 2057–2062.

37 Ho, K.H.W., Shang, A., Shi, F. et al. (2018). Hot carriers: plasmonic Au/TiO_2-dumbbell-on-film nanocavities for high-efficiency hot-carrier generation and extraction. *Adv. Funct. Mater.* 28: 1800383.

38 Hou, W., Hung, W.H., Pavaskar, P. et al. (2011). Photocatalytic conversion of CO_2 to hydrocarbon fuels via plasmon-enhanced absorption and metallic interband transitions. *ACS Catal.* 1: 929–936.

39 Aziz, M.A.A., Jalil, A.A., Triwahyono, S., and Ahmad, A. (2015). CO_2 methanation over heterogeneous catalysts: recent progress and future prospects. *Green Chem.* 17: 2647–2663.

40 Fu, G., Jiang, M., Liu, J. et al. (2021). Rh/Al nanoantenna photothermal catalyst for wide-spectrum solar-driven CO_2 methanation with nearly 100% selectivity. *Nano Lett.* 21: 8824–8830.

41 Fleischmann, M., Hendra, P.J., and McQuillan, A.J. (1974). Raman spectra of pyridine adsorbed at a silver electrode. *Chem. Phys. Lett.* 26: 163–166.

42 Jeanmaire, D.L. and Van Duyne, R.P. (1977). Surface Raman spectroelectro-chemistry. Part I. Heterocyclic, aromatic, and aliphatic amines adsorbed on the anodized silver electrode. *J. Electroanal. Chem.* 84: 1–20.

43 Nie, S.M. and Emory, S.R. (1997). Probing single molecules and single nanoparticles by surface-enhanced Raman scattering. *Science* 275: 1102–1106.

44 Kneipp, K., Wang, Y., Kneipp, H. et al. (1997). Single molecule detection using surface-enhanced Raman scattering (SERS). *Phys. Rev. Lett.* 78: 1667–1670.

45 Panneerselvam, R., Liu, G.K., and Wang, Y.H. (2018). Surface enhanced Raman spectroscopy bottle necks and future directions. *Chem. Commun.* 54 (10): 10–25.

46 Ke, S., Kan, C., Zhu, X. et al. (2021). Effective fabrication of porous Au-Ag alloy nanorods for in-situ Raman monitoring catalytic oxidation and reduction reactions. *J. Mater. Sci. Technol.* 91: 262–269.

47 Zhang, W.H., Cui, X.D., Yeo, B.S. et al. (2007). Nanoscale roughness on metal surfaces can increase tip enhanced Raman scattering by an order of magnitude. *Nano Lett.* 7 (5): 1401–1405.

48 Dantham, V.R., Holler, S., Barbre, C. et al. (2013). Label-free detection of single protein using a nanoplasmonic-photonic hybrid microcavity. *Nano Lett.* 13: 3347–3351.

49 Stockman, M.I. (2015). Nanoplasmonic sensing and detection. *Science* 348: 287–288.

50 Boriskina, S.V., Cooper, T.A., Zeng, L. et al. (2017). Losses in plasmonics from mitigating energy dissipation to embracing loss-enabled functionalities. *Adv. Opt. Photonics* 9: 775–827.

51 Clavero, C. (2014). Plasmon-induced hot-electron generation at nanoparticle/metal-oxide interfaces for photovoltaic and photocatalytic devices. *Nat. Photonics* 8 (2): 95–103.

52 Zhang, Y., He, S., Guo, W. et al. (2018). Surface-plasmon-driven hot electron photochemistry. *Chem. Rev.* 118: 2927–2954.

53 Tang, H., Chen, C.J., Huang, Z. et al. (2020). Plasmonic hot electrons for sensing, photodetection, and solar energy applications: a perspective. *J. Chem. Phys.* 152: 220901.

54 Mukherjee, S., Libisch, F., Large, N. et al. (2013). Hot electrons do the impossible: plasmon-induced dissociation of H_2 on Au. *Nano Lett.* 13: 240–247.

55 Chen, C.L., Zhou, L., Yu, J.Y. et al. (2018). Dual functional asymmetric plasmonic structures for solar water purification and pollution detection. *Nano Energy* 51: 451–456.

56 Liang, J., Liu, H.Z., Yu, J.Y. et al. (2019). Plasmon enhanced solar vapor generation. *Nanophotonics* 8 (5): 771–786.

57 Zhou, L., Tan, Y.L., Ji, D.X. et al. (2016). Self-assembly of highly efficient broad band plasmonic absorbers for solar steam generation. *Sci. Adv.* 2 (4): e1501227.

58 Zhu, M.W., Li, Y.J., Chen, F.J. et al. (2018). Plasmonic wood for high efficiency solar steam generation. *Adv. Energy Mater.* 8 (4): 170102.

59 Brongersma, M.L., Halas, N.J., and Nordlander, P. (2015). Plasmon-induced hot carrier science and technology. *Nat. Nanotechnol.* 10: 25–34.

60 Hartland, G.V. (2011). Optical studies of dynamics in noble metal nanostructures. *Chem. Rev.* 111: 3858–3887.

61 Kale, M.J., Avanesian, T., Xin, H. et al. (2014). Controlling catalytic selectivity on metal nanoparticles by direct photoexcitation of adsorbate-metal bonds. *Nano Lett.* 14: 5405–5412.

62 Wu, K., Chen, J., McBride, J.R., and Lian, T. (2015). Efficient hot-electron transfer by a plasmon-induced interfacial charge-transfer transition. *Science* 349: 632–635.

63 Stockman, M.I. (2020). Brief history of spaser from conception to the future. *Adv. Photonics* 2: 054002.

64 Okamoto, K., Niki, I., Shvartser, A. et al. (2004). Surface-plasmon-enhanced light emitters based on InGaN quantum wells. *Nat. Mater.* 3 (9): 601–605.

65 Oulton, R.F., Sorger, V.J., Genov, D.A. et al. (2008). A hybrid plasmonic wave guide for subwavelength confinement and long-range propagation. *Nat. Photonics* 28: 496–500.

66 Oulton, R.F., Sorger, V.J., Zentgraf, T. et al. (2009). Plasmon lasers at deep subwavelength scale. *Nature* 461: 629–632.

67 Ma, R., Oulton, R.F., Sorger, V.J., and Zhang, X. (2013). Plasmon lasers: coherent light source at molecular scales. *Laser Photonics Rev.* 7 (1): 1–21.

68 Lu, Y.J., Wang, C.Y., Kim, J. et al. (2014). All-color plasmonic nanolasers with ultralow thresholds: autotuning mechanism for single-mode lasing. *Nano Lett.* 14: 4381–4388.